High Reliability ArF Light Source for Double Patterning Immersion Lithography

Rostislav Rokitski; Toshi Ishihara; Rajeskar Rao; Rui Jiang;
Mary Haviland; Theodore Cacouris; Daniel Brown, Cymer Inc.

ABSTRACT

Double patterning lithography places significant demands not only on the optical performance of the light source (higher power, improved parametric stability), but also on high uptime in order to meet the higher throughput requirements of the litho cell. In this paper, we will describe the challenges faced in delivering improved performance while achieving better reliability and resultant uptime as embodied in the XLR 600ix light source from Cymer, announced one year ago. Data from extended life testing at 90W operation will be shown to illustrate these improvements.

KEYWORDS: immersion lithography, double patterning, excimer laser, deep ultraviolet

1. INTRODUCTION

Double patterning (DP) lithography is gaining widespread use in 32 and sub-32nm technology nodes as an extension to immersion lithography. While many resolution enhancement technologies (RET) have been developed recently, including source-mask optimization (SMO)[1], and pixilated illumination[2] schemes for the scanner, the overarching requirement for the light source in double patterning has been a need for improved optical performance stability and higher power. With the introduction of the XLR 600ix light source from Cymer last year, these requirements have been met and integrated on the most advanced DP immersion scanners on the market. Key areas of improvement include higher power with flexibility to address a wide range (60 to 90W), improved energy stability, improved bandwidth stability and improved wavelength stability. The details of these improvements were reported on a previous paper[3]. These characteristics have enabled improved CD uniformity along with higher throughput operation for the litho cell to counteract the impact of the higher cost of DP lithography.

In addition to providing improved performance, the light source needs to have higher reliability and uptime in a DP environment, as the impact of down time is magnified further when the litho cell throughput is increased dramatically. In this area, the XLR 600ix was designed to address this need by building on a proven platform and introducing features that further enhance reliability and uptime. In this paper, we will describe the challenges faced in delivering improved performance while achieving better reliability and uptime on the XLR 600ix. Areas of improvement include development of advanced optics materials and coatings to provide stable performance over a wide power range (60 to 90W), an improved control system delivering faster closed-loop feedback for optical stability over extended periods, and 'smart' on-board diagnostics with predictive capability to prevent unscheduled downtime. Data from extended life testing as well as field performance data will be presented to illustrate these improvements.

2. TECHNOLOGY ADVANCEMENTS

Several technologies have been introduced in this light source to enable not only high power operation, but sustained performance stability under continuous operation at high power. The development of optical materials and coatings that can endure fluences in excess of 20mJ internal to the light source (in order to deliver an output of 15mJ) while staying impervious to thermal effects has been a key enabling technology. Similarly, advanced control algorithms that further reduce parametric variability in wavelength, bandwidth and energy have enabled the use of fewer pulses to achieve a desired on-wafer dose stability, which in turn leverages the use of higher energy to improve wafer throughput at the scanner. An example of such performance improvements is shown for four different light sources tested under varying repetition (rep) rates from 1.5 to 6kHz in Figure 1, where energy stability is measured.

Optical Microlithography XXIII, edited by Mircea V. Dusa, Will Conley, Proc. of SPIE Vol. 7640,
76401Q · © 2010 SPIE · CCC code: 0277-786X/10/$18 · doi: 10.1117/12.849065

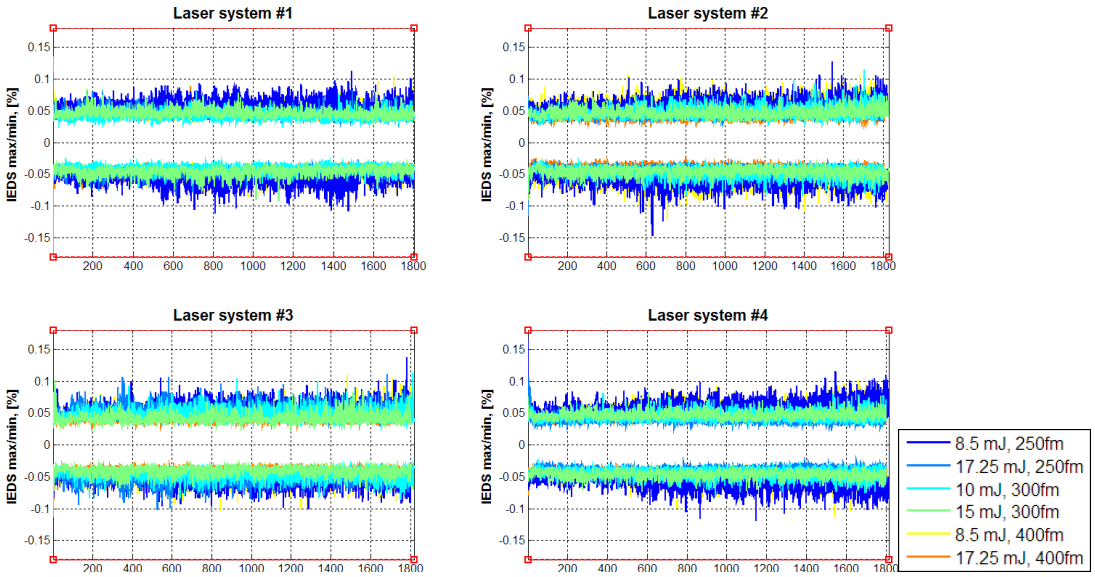

Figure 1 – Dose stability of 4 different light sources measured across various energy and bandwidth settings varying from 8.5mJ (51W) to 17.25mJ (103.5W), which covers the nominal 60 – 90W operation. The horizontal axis represents a sequence of 'bursts' or firing patterns of the test suite that include variations in rep rate, starting with 6kHz (leftmost data) and decreasing to 1.5kHz.

More recently, a new advancement in excimer laser discharge chamber technology was introduced in the XLR 600ix to further improve performance stability over life. Excimer discharge chambers have a finite operating life that is modulated by several key aging mechanisms: (a) discharge electrode erosion, (b) chamber window damage due to DUV exposure, and (c) accumulation of particulate debris, or 'dust' that are byproducts of gas interaction with chamber materials. While advances in chamber design and material selection have progressively extended the life of discharge chambers by minimizing or mitigating the aging mechanisms, they have not fundamentally addressed the observed trending of operating parameters that result from aging. For example, while electrode erosion rates can be reduced with the appropriate selection of materials and design, the change in electrode gap due to erosion is still present and can result in beam property changes over time. The new technology recently introduced with the XLR 600ix includes a new discharge chamber design that automatically compensates for electrode erosion by simply moving the electrodes physically to maintain a constant gap (Figure 2). While this concept is not new, the ability to realize it in a production-worthy light source has been elusive until now. The benefit of maintaining a constant gap between electrodes in the discharge chamber is a more stable beam characteristic in physical dimensions, and the secondary effects that can contribute to parametric stability. This translates to better stability in pupil fill, less variation in bandwidth and a resulting improved focus, overlay and CD control on the wafer.

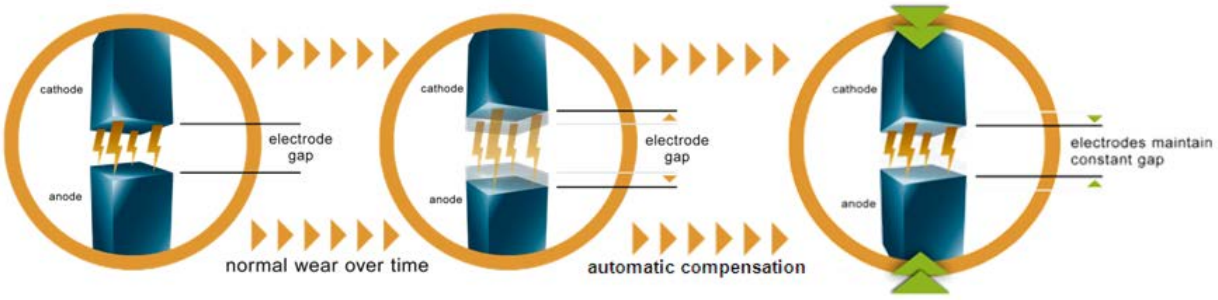

Figure 2 – Discharge chamber electrode aging results in a change in the electrode gap over time; new chamber technology recently introduced automatically compensates for this effect to maintain a constant gap as illustrated here, resulting in more stable performance over the life of this chamber.

3. EXTENDED RELIABILITY TESTING

While performance testing and reliability have been extensively demonstrated for light sources operating at 10mJ, 6kHz (60W), this is the first instance where extensive testing has been performed and demonstrated on a light source running 15mJ, 6kHz (90W). Previous reports on the XLR 600ix have centered on the challenges of maintaining improved light source stability while achieving higher power (90W). We report here, for the first time, extensive testing that represents ~ 1year of continuous operation at a high utilization memory fab.

In the aforementioned extended testing, a XLR 600ix light source operating at 90W was subjected to continuous operation similar to a high utilization fab environment, simulating about 1 year of operation. This testing was performed in an accelerated manner to enable completion of this test within 30 weeks, accumulating 30 billion pulses of DUV light. Interspersed with the continuous operation were periodic test suites that collected detailed parametric data to monitor light source performance. Figure 3 illustrates an example of this data set where wavelength stability is analyzed in terms of average wavelength error around the central wavelength, where the data is clustered mostly within ±5fm compared to a performance requirement for the scanner of ±12fm. Improved wavelength stability directly affects on-wafer contrast and focus, that results in improved CD uniformity.

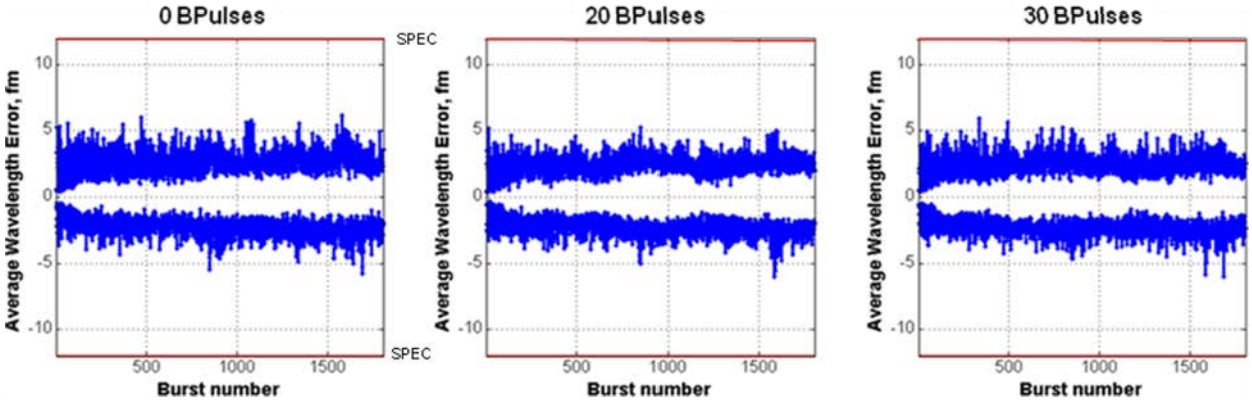

Figure 3 – Average wavelength error measured at the beginning of the extended test (0 Bpulses), at 20Bpulses and at the end of the test (30Bpulses). Wavelength error remains unchanged and mostly clustered within ±5fm around the center wavelength. The horizontal axis represents a sequence of 'bursts' or firing patterns of the test suite that include variations in rep rate, duty cycle and energy to test the effects of wavelength stability across all operating conditions.

The test suites used to evaluate light source performance periodically include subjecting the light source to variations in rep rate, duty cycle and energy to capture the performance across all operating space. Figure 4 further explores wavelength stability through wavelength sigma, indicating that most of the data across all operating conditions is clustered below 30fm, with a scanner requirement of <50fm for this technology generation.

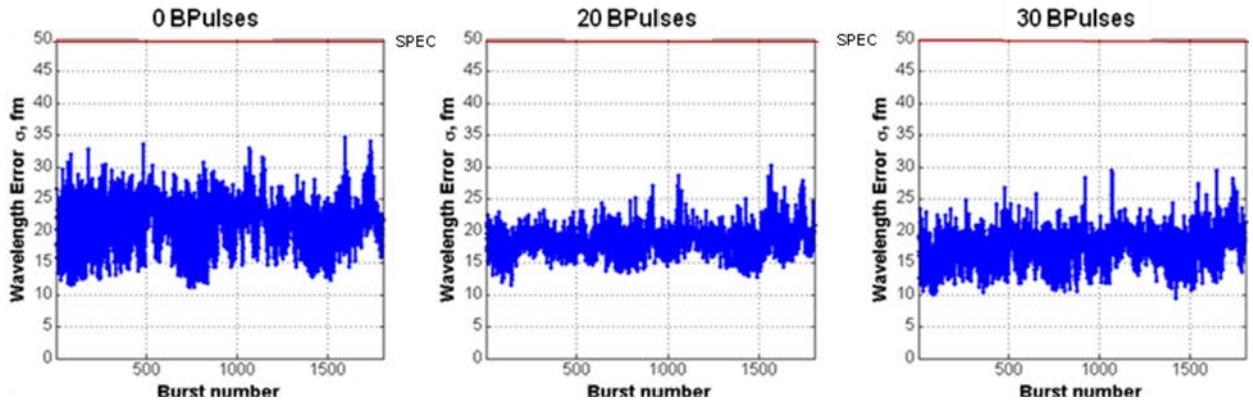

Figure 4 – Wavelength sigma measured at the beginning of the extended test (0 Bpulses), at 20Bpulses and at the end of the test (30Bpulses). Wavelength sigma remains unchanged and mostly clustered below 30fm. The horizontal axis represents a sequence of 'bursts' or firing patterns of the test suite that include variations in rep rate, duty cycle and energy to test the effects of wavelength stability across all operating conditions.

In addition to wavelength stability measurements, bandwidth stability was similarly evaluated, as shown in Figure 5. Here, the nominal bandwidth target is 300fm and is maintained through the use of active controls to support optical proximity correction (OPC) design features in the mask set with minimal variation. This in turn results in the high contrast necessary on-wafer to achieve the desired CD uniformity. The data shown in Figure 5 shows that throughout the extensive testing, the nominal bandwidth stays centered at 300fm and the variation observed across varying operating conditions (rep rate, duty cycle and energy) are mostly within 25fm.

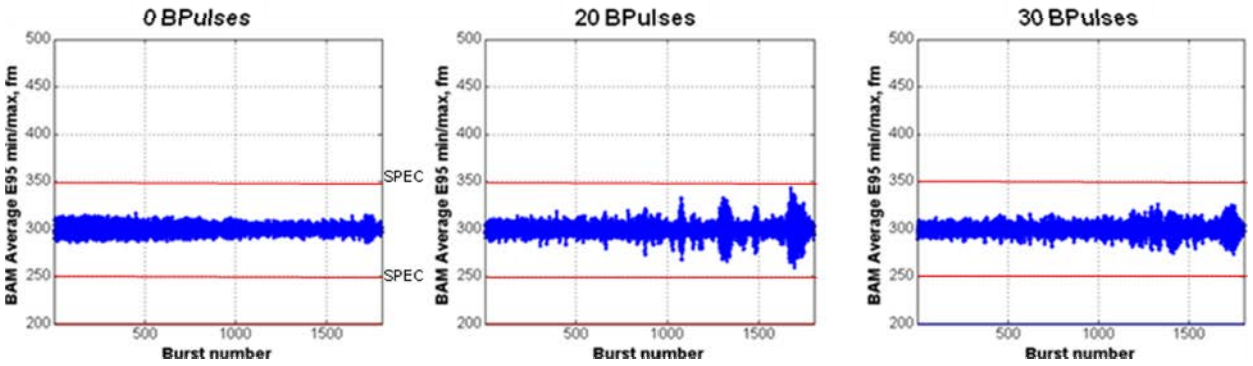

Figure 5 – Bandwidth stability measured at the beginning of the extended test (0 Bpulses), at 20Bpulses and at the end of the test (30Bpulses). Nominal bandwidth target is remains unchanged at 300fm and bandwidth variation is mostly within 25fm. The horizontal axis represents a sequence of 'bursts' or firing patterns of the test suite that include variations in rep rate, duty cycle and energy to test the effects of bandwidth stability across all operating conditions.

Energy stability was also monitored throughout the extended testing and the calculated dose stability based on a 35-pulse window was well below ±0.1%, especially at the high rep rates (Figure 6). Raw energy sigma also showed low values, mostly below 3%, with some deviations to 4% at the lower rep rates and near the end of the test period (Figure 7).

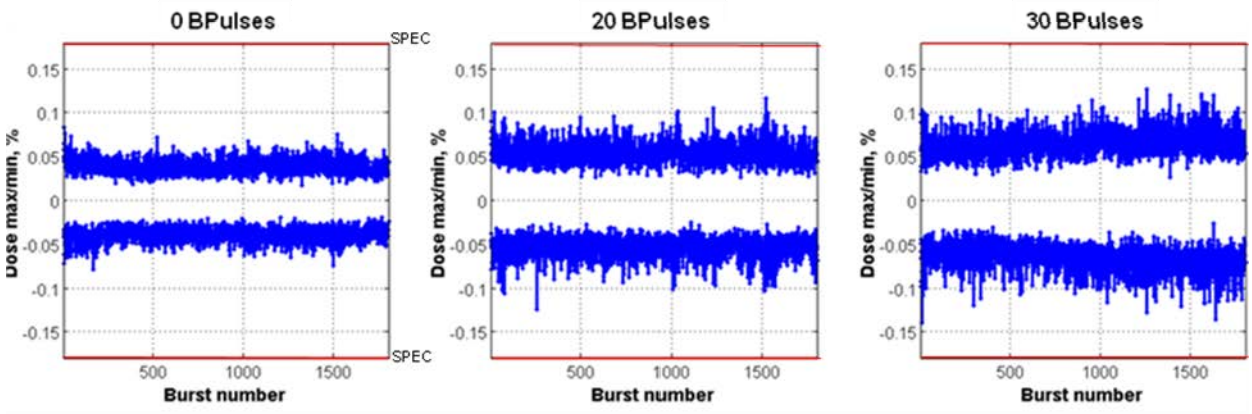

Figure 6 – Dose stability measured at the beginning of the extended test (0 Bpulses), at 20Bpulses and at the end of the test (30Bpulses). Dose variation is mostly below ±0.1%, especially at the high rep rates (6kHz) that are captured at the leftmost set of data. The horizontal axis represents a sequence of 'bursts' or firing patterns of the test suite that include variations in rep rate, duty cycle and energy to test the effects of bandwidth stability across all operating conditions.

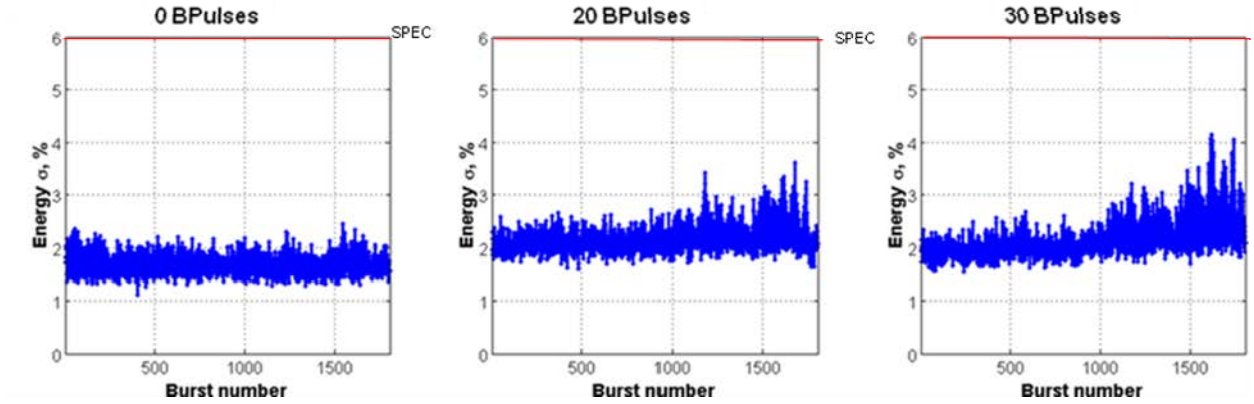

Figure 7 – Raw energy stability (sigma) measured at the beginning of the extended test (0 Bpulses), at 20Bpulses and at the end of the test (30Bpulses). Energy sigma is mostly below 3%, especially at the high rep rates (6kHz) that are captured at the leftmost set of data. The horizontal axis represents a sequence of 'bursts' or firing patterns of the test suite that include variations in rep rate, duty cycle and energy to test the effects of bandwidth stability across all operating conditions.

4. PERFORMANCE MONITORING

While fundamental improvements in performance and reliability have been introduced with this light source, a complementary, an operational infrastructure is key in maximizing uptime and utilization. In particular, serviceability and maintainability of the light source can dramatically enhance the litho cell performance with better performance and productivity. Cymer light sources have historically been 'connected' to provide near-real-time performance data to a centralized monitoring station. Initially, this connectivity enabled remote monitoring by experts who could better direct field service personnel on a particular maintenance activity, based on symptoms and their experience. Statistical-process-control (SPC) type charting augmented this capability by flagging light sources that were showing signs of less than ideal performance, helping proactively schedule maintenance before an unscheduled event occurred. More recently, we introduced algorithms that mine this data to extract unique performance signatures, essentially automating the analysis and providing specific guidance to the field service engineer. The on-board light source control system continuously monitors the system state for anomalous behavior. When an anomaly is encountered, a high-data-rate log of key signals is automatically sent to the central monitoring station. Sophisticated fault-signature detection (FSD) algorithms that reside on the central station that employ

pattern recognition functions analyze this data to identify known patterns associated with a particular subsystem. As this data is amassed, a picture of the health of the system is developed and a maintenance action can be scheduled to proactively correct the issue. The net result of this approach is that fewer unscheduled events occur, and when a maintenance action is required, it can be scheduled to ensure the proper resources and parts are in place to minimize down time (Figure 8).

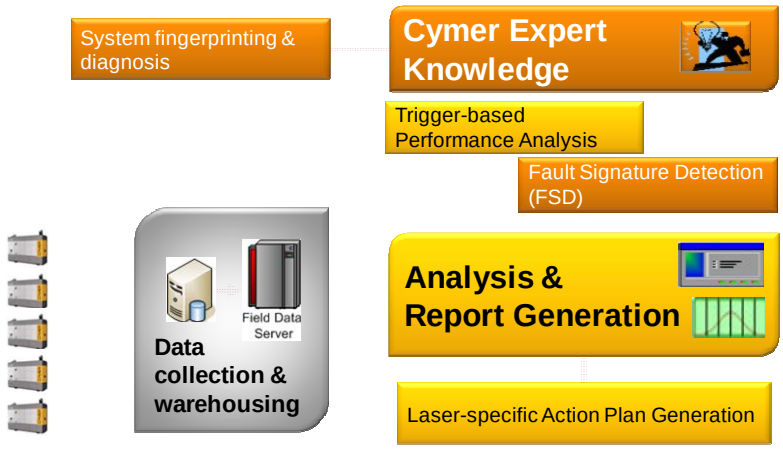

Figure 8 – Down time reduction through automation of data analysis of light source performance data. Centralized data collection and warehousing enables the use of fault signature detection (FSD) to automate knowledge derived from laser experts, which can trigger a scheduled maintenance action. Continuous diagnostics generation shortens or eliminates the time required to troubleshoot a fault.

In parallel, a routine that runs periodically on the light source collects a 'fingerprint' or performance state of the system which can be used during a service event to quickly identify the source of degraded performance, thereby minimizing the time required for troubleshooting. This function tracks key performance indicators so that once a service event is concluded, the light source can be restored back to its 'healthy' state.

5. SUMMARY

As 193nm immersion lithography is further challenged with double patterning applications, stringent demands are placed on the light source to enable improved CD uniformity, overlay and OPC performance. The XLR 600ix light source described here exceeds these requirements and further enhances the lithographer's toolbox by providing flexibility in power output. Demonstrated extended performance at 90W supports the requirements of high-throughput double patterning applications, where high uptime and utilization are expected. Such high uptime has been achieved through the use of new optics and chamber technology, as well as a data infrastructure and analysis capability.

[1]Matsuyama, T., Nakashima, T., Noda, T., "A study of source and mask optimization for ArF scanners," Proc. SPIE 7274 (2009)

[2]Lai, K., Rosenbluth, A. E., Bagheri, S., Hoffnagle, J. A., Tian, K., Melville, D. O., Tirapu-Azpiroz, J., Fakhry, M., Kim, Y., Halle, S. D., McIntyre, G., Burr, G. W., Burkhardt, M., Corliss, D. A., Flagello, D. G., Zimmermann, J., Kneer, B., Rohmund, F., Hartung, F., Russ, C., Maul, M., Kazinczi, C. R., Engelen, A., Mulder, M., "Experimental result and simulation analysis for the use of pixelated illumination from source mask optimization for 22-nm logic lithography process", Proc. SPIE 7274 (2009).

[3] Rokitski, R., Ishihara, T., Rao, R., Jiang, R., Riggs, D., Haviland, M., Cacouris, T., Brown, D., “Flexible 60-90W ArF light source for double patterning immersion lithography in high volume manufacturing”, Proc. SPIE Lithography Asia 7520-37 (2009).

Laser bandwidth effect on overlay budget and imaging for the 45 nm and 32nm technology nodes with immersion lithography

Umberto Iessi [a], Michiel Kupers[b], Elio De Chiara[a] Pierluigi Rigolli[a], Ivan Lalovic[c],G. Capetti[a]
[a] Numonyx, Via C. Olivetti 2, Agrate Brianza (MI) 20041, Italy
[b]Cymer B.V., De Run 4312B, 5503 LN Veldhoven, Netherlands
[c]Cymer, Inc., 17075 Thornmint Court, San Diego, CA 92127

ABSTRACT

The laser bandwidth and the wavelength stability are among the important factors contributing to the CD Uniformity budget for a 45 nm and 32nm technology node NV Memory. Longitudinal chromatic aberrations are also minimized by lens designers to reduce the contrast loss among different patterns. In this work, the residual effect of laser bandwidth and wavelength stability are investigated and quantified for a critical DOF layer. Besides the typical CD implications we evaluate the "image placement error" (IPE) affecting specific asymmetric patterns in the device layout. We show that the IPE of asymmetric device patterns can be sensitive to laser bandwidth, potentially resulting in nanometer-level errors in overlay. These effects are compared to the relative impact of other parameters that define the contrast of the lithography image for the 45nm node. We extend the discussion of the contributions to IPE and their relative importance in the 32 nm double-patterning overlay budget.

Keywords: CD Uniformity, Overlay Budget. Lens Aberrations, Laser bandwidth, Image Placement error

1. INTRODUCTION

As the industry heads towards ever smaller feature sizes and complex pattern layouts, sources of imaging and overlay errors that were neglected in the past are now becoming increasingly significant. In this paper we will investigate the impact of laser bandwidth on CD and the image placement error of asymmetric device patterns. Although the CD imaging effects have been explored before, for example in a paper by Bisschop et. al. (see reference [3]), here we will apply methods to specifically quantify the image placement effects for specific asymmetric device patterns for NV Memory (see reference [1]). This pattern was printed with a 6%-attenuated Phase Shift Mask at NA=1.20 using dipole illumination at 193nm wavelength. The dipole was horizontally oriented and had 60-deg opening angle, radially delimited by SigmaInner=0.65, SigmaOuter=0.85. The exposure-light was polarized in y-direction.

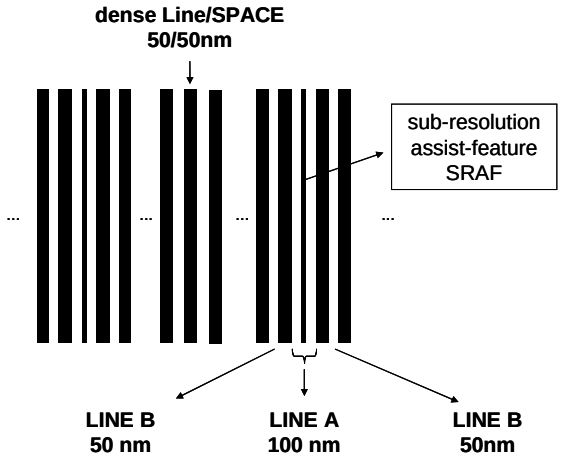

Figure 1: Pattern to be printed: Dense lines and spaces with pitch-interruption. Investigated are Critical Dimensions CD of 'LINE A', 'LINE B' and 'SPACE'. Dimensions indicated in the figure are target-values.

Optical Microlithography XXIII, edited by Mircea V. Dusa, Will Conley, Proc. of SPIE Vol. 7640,
76402B · © 2010 SPIE · CCC code: 0277-786X/10/$18 · doi: 10.1117/12.846552

Furthermore, we will use simulation software to study the impact of laser bandwidth on CD as well as on the Image Placement Error (IPE) and the relative contributions of the higher order Zernike coefficients. A recent update in the Panoramic™ lithography simulation software now makes it possible to directly calculate the impact of the higher-order chromatic aberrations. The resulting aerial image is calculated by sampling the spectrum at discrete wavelength points. A set of aerial images is obtained with each image corresponding to a single wavelength sample. Finally, the images are weighted by the intensity in the laser spectrum at the corresponding wavelength and summed together. This computation method has been described before, for example references [3,4], and is described schematically in the figure below. In our case, the individual aerial images are computed with different aberration levels as defined by a set of Z4-Z37 Zernike coefficients corresponding to each discrete wavelength sample.

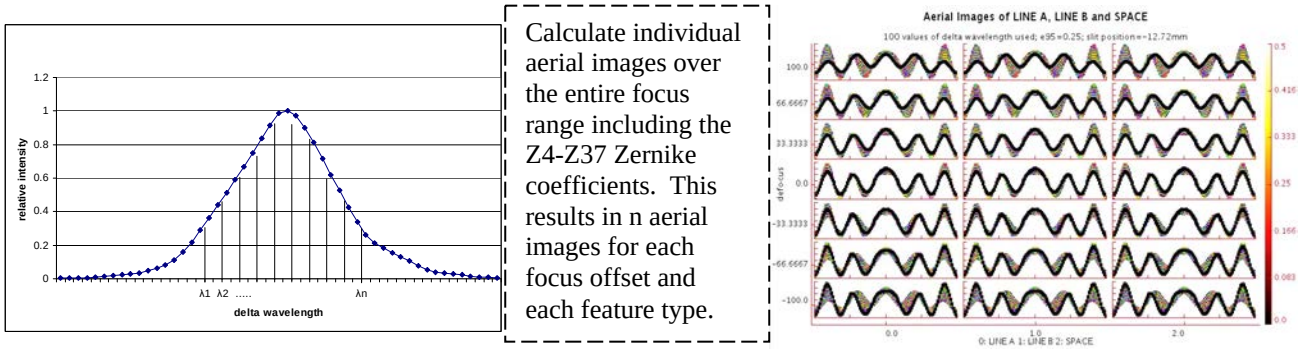

In this study, the aggregate aerial image is calculated using a typical spectrum from a Cymer XLA360 laser, which is shown in Figure 2.

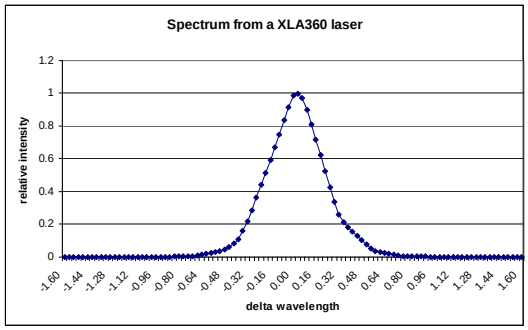

Figure 2 XLA360 spectrum used as a weighting function for the simulations.

A previous study has quantified the effect of IPE as a function different overlay marks (see reference [2]). Although these effects are quite small, we have extended this work to study the effect of the higher order chromatic aberrations for the AIM overlay marks used for this particular layer

1.1 Impact of higher order aberrations on IPE

Higher order aberrations are commonly defined as the Z5 to Z37 Zernike polynomial terms that describe deformations from spherical wavefronts (see for example reference [6]). In prior studies, it has been shown that the IPE is mostly affected by the lower order terms and it was assumed that higher order terms are small and can be neglected. Our simulation will quantify the magnitude of the contributions of the higher order terms for the particular features described above.

2. SIMULATIONS

2.1 IPE simulations for 45 nm node

For our simulations we will use Hyperlith™ from Panoramic Inc. The following inputs were used:

- GDS data from the reticle using 0.5 nm of simulation grid
- NA: 1.2 ; sigma inner=0.85 sigma outer=0.65, using X 60º dipole (Y polarized)
- Used -350 nm/pm as chromatic sensitivity

- Used measured Zernike data at 3 wavelengths (0, -0.5pm, +0.5pm) from an ASML XT1700i scanner in the Numonyx Fab. Due to confidentiality reasons we will not disclose the exact numbers.
- +/- 10% and +/- 100 nm of aerial image threshold and focus variation applied respectively.
- The image threshold is anchored to the SPACE feature

The results are shown in the plots of Figure 3 and Figure 4. Note that the plots are a function of focus and slit position. Except for LINE A, the variation of the IPE in the slit due to the higher order Zernikes is quite small. LINE B is more sensitive to focus variations than LINE A. In Figure 4 we show the variation of the IPE through the slit for the different types of pattern. These values are confirmed by an overlay experiment, and we discuss these results in section 3.4.

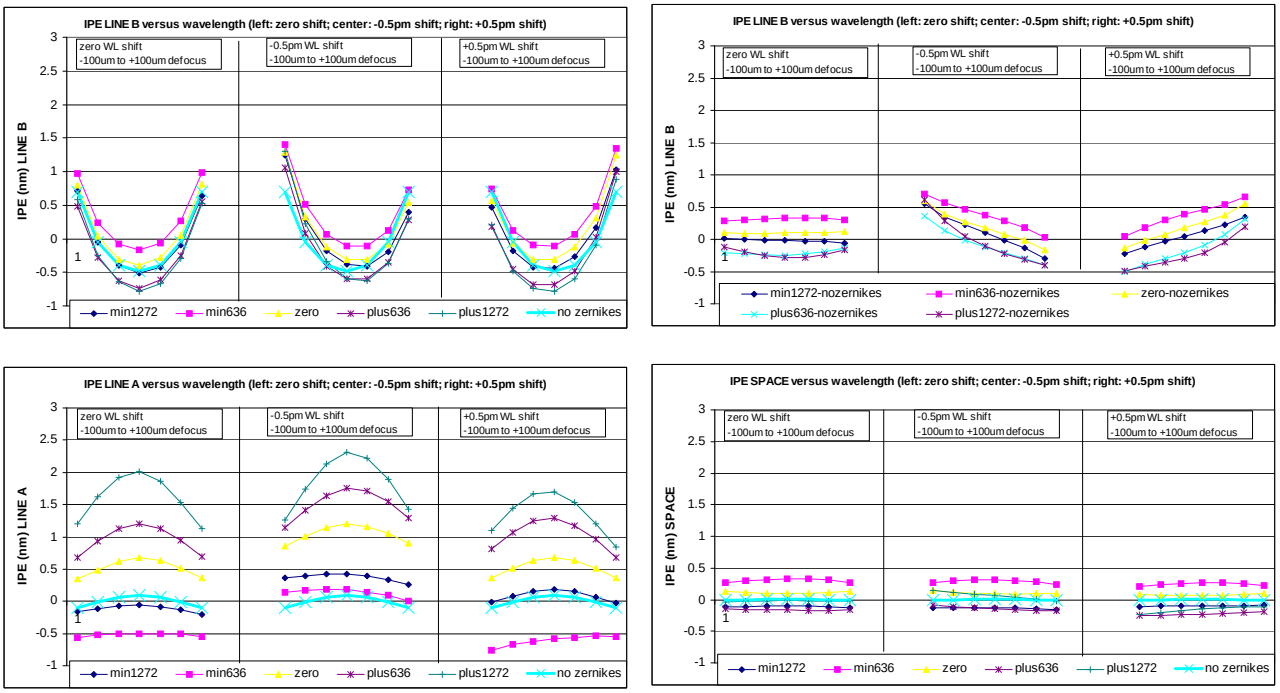

Figure 3: IPE (nm) through focus, slit position, wavelength and feature type. The wavelength of the laser was changed by -0.5pm and +0.5pm. From left to right and top to bottom: IPE LINE B through focus and wavelength; the change in IPE through focus when the no Zernike case is subtracted; IPE LINE A through focus and wavelength; IPE SPACE through focus and wavelength

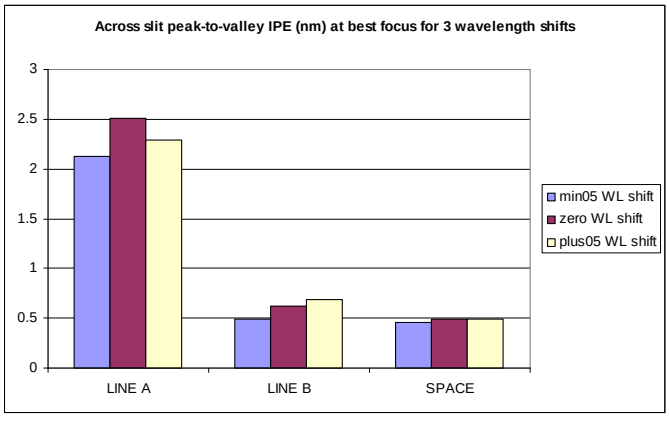

Figure 4 : total IPE variation over the slit for 3 types of patterns

To investigate the effect of chromatic aberrations and finite laser bandwidth on IPE, we will now generalize this approach and consider the aggregate aerial images computed over a range of wavelengths. To do this we must obtain the Zernike coefficients as a function of wavelength. The Zernike sensitivities to wavelength for this optical lithography scanner where determined experimentally, by measuring the aberrations at several wavelength set-points. These Zernike coefficients are typically linear with the wavelength, over a range of several picometers of wavelength offsets from nominal, which means we can perform interpolation to determine a range of intermediate values. Previous studies (reference [3] and [7]) have discussed the sampling requirements in order to accurately simulate the effect of bandwidth when using the defocus or Z4 aberration term only. Since it is rather easy to program the number of interpolations in the simulation software we have chosen to interpolate and calculate the aggregate aerial image over 100 samples of wavelength shift. . We also consider 6 values of the E95 laser bandwidth: 0.00pm, 0.25pm, 0.32pm, 0.38pm, 0.50pm and 1.00pm. We have included the e95=1.0pm value in order to assess the effect of bandwidth significantly beyond the usual operating range of lasers such as the XLA360 (see section 3.4 for a discussion on this).
To get an accurate description of the behavior of IPE versus bandwidth with and without the higher order Zernikes, we will compute the IPE at 5 different positions in the slit as well as through focus (-100um to +100um). The results for LINE B are plotted in Figure 5. Similar plots can be made for the other features. Figure 6 and Figure 7 show the IPE at best focus for LINE B, LINE A and SPACE for all the E95 values as well as the case where the Zernike coefficients are absent from the simulation. We see that LINE B is most sensitive to bandwidth whereas LINE A is mostly sensitive to the higher order Zernikes. In Figure 8 we show the variation of IPE over the slit as a function of bandwidth when we also consider the impact of the lower order Zernikes (Z2, Z3, Z4). From Figure 5 we see that the IPE for the most sensitive pattern, LINE B, changes by 0.9nm to 1.5 nm (depending on focus) over the 1pm change in BW. The other patterns are not sensitive to bandwidth. Note that the IPE effect is significantly lower over the typical bandwidth operating ranges of the XLA 360 laser, namely about 0.2nm to 0.5nm at extremes of defocus. The effect is even lower for laser systems that feature active bandwidth stabilization, such as the XLR 560i.

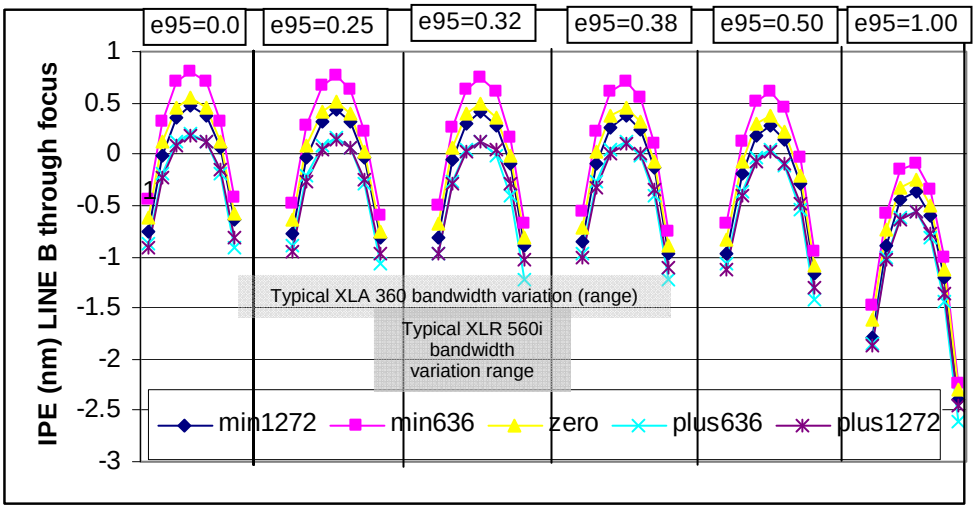

Figure 5: IPE as a function of laser bandwidth for LINE B through focus (-100nm,-66nm,-33nm, 0, +33nm, +66nm, +100nm)

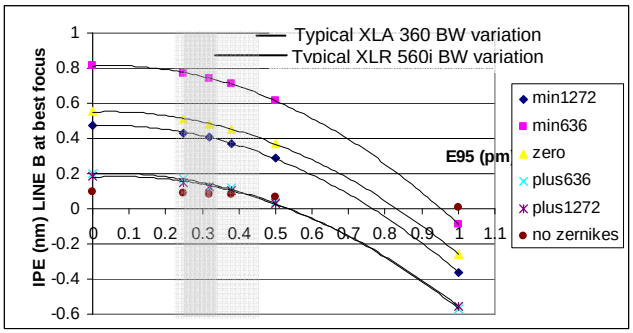

Figure 6: IPE as a function of bandwidth for LINE B. The bandwidth variation range for the XLA 360 laser type used in these experiments is shown in the shaded area; the typical bandwidth variation for XLR 560i systems featuring advanced bandwidth stabilization is also included for comparison

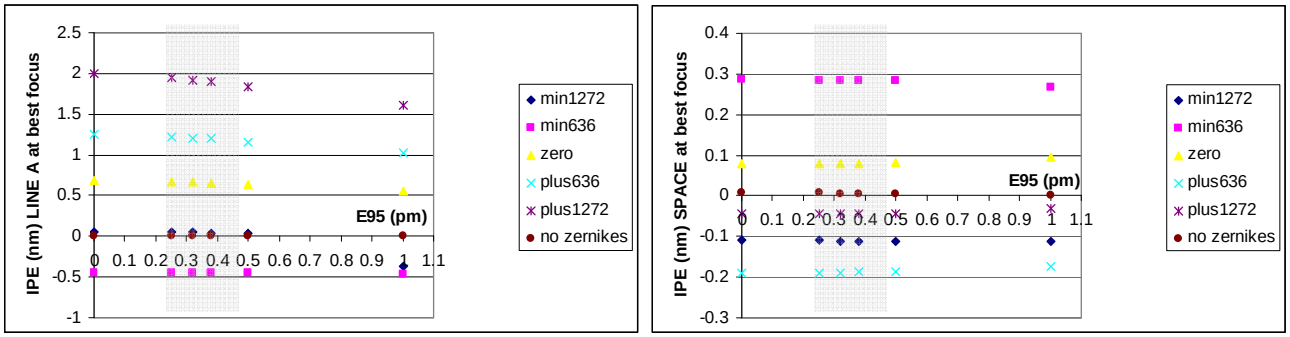

Figure 7: IPE as a function of laser bandwidth for LINE A and SPACE. The bandwidth variation range for the XLA 360 laser type used in these experiments is shown in the shaded area

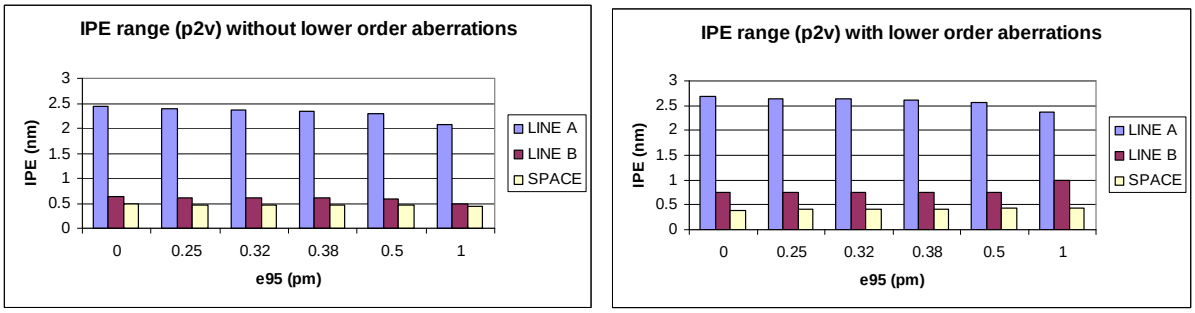

Figure 8: Across-slit IPE range at best focus with and without the lower order aberrations as a function of laser bandwidth for LINE A, LINE B and SPACE

2.2 IPE simulations for 32 nm node

The 32 nm lithography step for NV Memories require the introduction of Self Align Double Patterning (SADP) methods. With this technique, it could be necessary to print asymmetric patterns in order to obtain the final desired structure after spacer definition. In our case study we evaluate the IPE of a pattern named "L" (see Figure 9) with different lens NA :1.2 immersion and 0.93 dry.

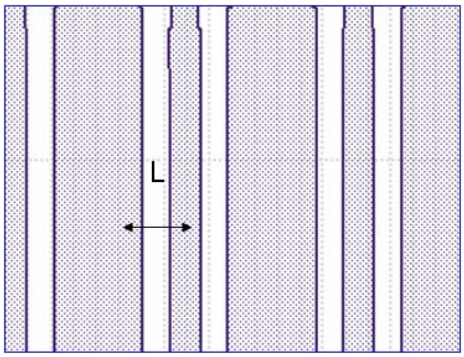

Figure 9: asymmetric layout for a 32nm technology node SADP memory device

The lithography pitch for a 64 nm SADP device is the half of the final patterned one so that dry lithography can be sufficient. Figure 10 shows that IPE is less than 0.2 nm and it is not sensitive to defocus. The relaxed k1 factor for both dry and immersion process (0.31 and 0.4 respectively) is protecting this technology node from IPE issues.

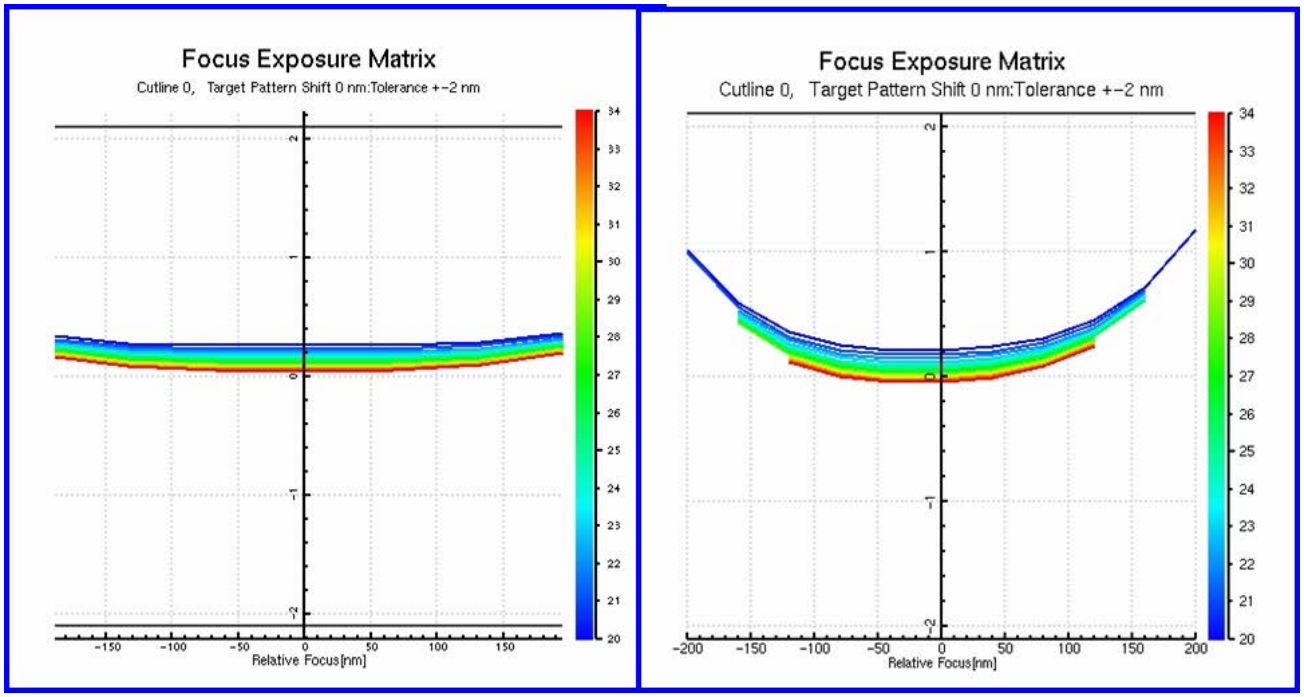

Figure 10: IPE(nm) through focus for the "L" pattern at different exposure doses

2.3 CD Uniformity simulations for 45 nm node

In order to evaluate the impact of laser bandwidth on our critical patterns we use ASML LithoCruiser Software to run simulations including in the model the appropriate scanner lens and illuminator fingerprint and a calibrated resist model.

This software first calculates the sensitivities of critical patterns to the main scanner parameters and than estimates a CDU budget for each of this main contributors in an early immersion lithography litho cell.

	Line A 3σ (nm)	Line B 3σ (nm)	Space 3σ (nm)
All	**3.05**	**2.78**	**2.30**
Scanner	0.52	0.83	0.26
Laser	**0.91**	**0.07**	**0.44**
Reticle	2.27	2.00	1.41
Process	1.51	1.51	1.51
Other	0.88	0.87	0.87

Table 1: CD uniformity for LINE A, LINE B and SPACE for each main contributor

The laser bandwidth contribution sensitivity is calculated by varying the bandwidth FWHM around the nominal value of 0.12 pm (equivalent to e95=0.25pm) and considering the defocus term only.

The laser bandwidth FWHM is varied over a range of 0.04 pm (0.08pm to 0.16 pm) and the model of the spectrum is a Modified Lorentzian with “n” factor equal to 3.6.

From Figure 11 we can conclude that, depending on the pattern, the laser contribution to the total CDU budget can be about 10%. LINE B is less affected by the laser contribution than the other patterns.

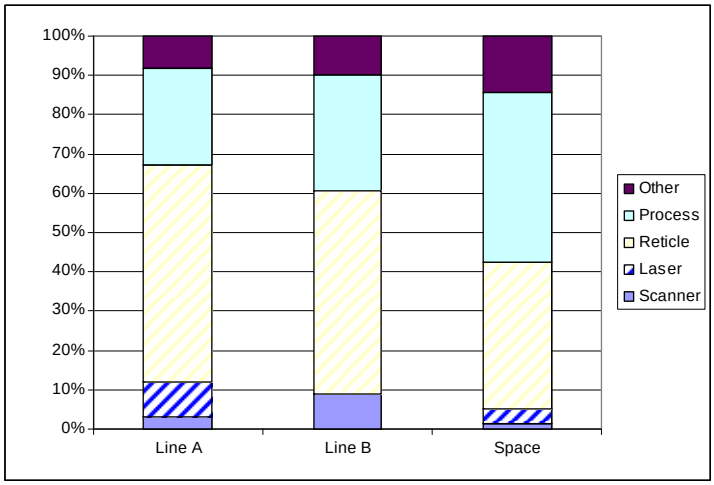

Figure 11: CDU budget for the different patterns and contributors

2.4 DOF simulation vs Laser Bandwidth

We determined the process window for the 3 different patterns for different typical conditions of the laser bandwidth. The depth of focus and exposure latitude of the overlapping process window is shown in **Table 2**.

Setting	FWHM (pm)	E95 (pm)	DOF (nm)	EL at 10% CD (nm)
A	0.12	0.25	86	19
B	0.22	0.37	64	18
C	0.33	0.5	34	6

Table 2: Elliptical DOF and EL for different laser bandwidth setting of FWHM and E95

Conditions “A” and “B” can be considered as the range of bandwidth used for normal operation. Within this range a consistent DOF reduction of about 14% can be explained by the high sensitivity of the LINE B pattern to defocus as can be seen in Figure 12. We will perform an experiment to confirm these results.

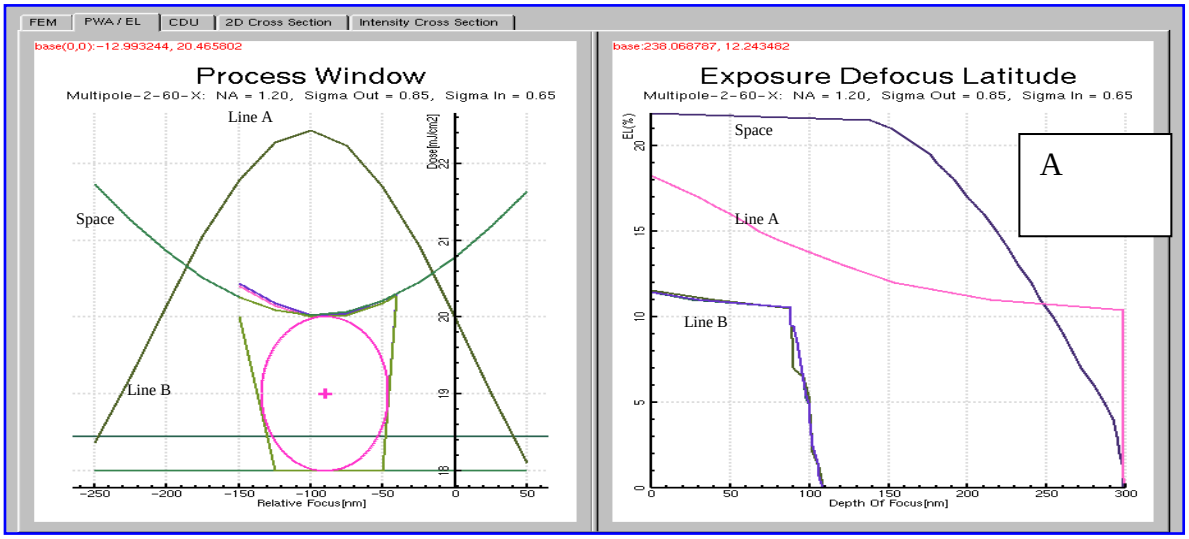

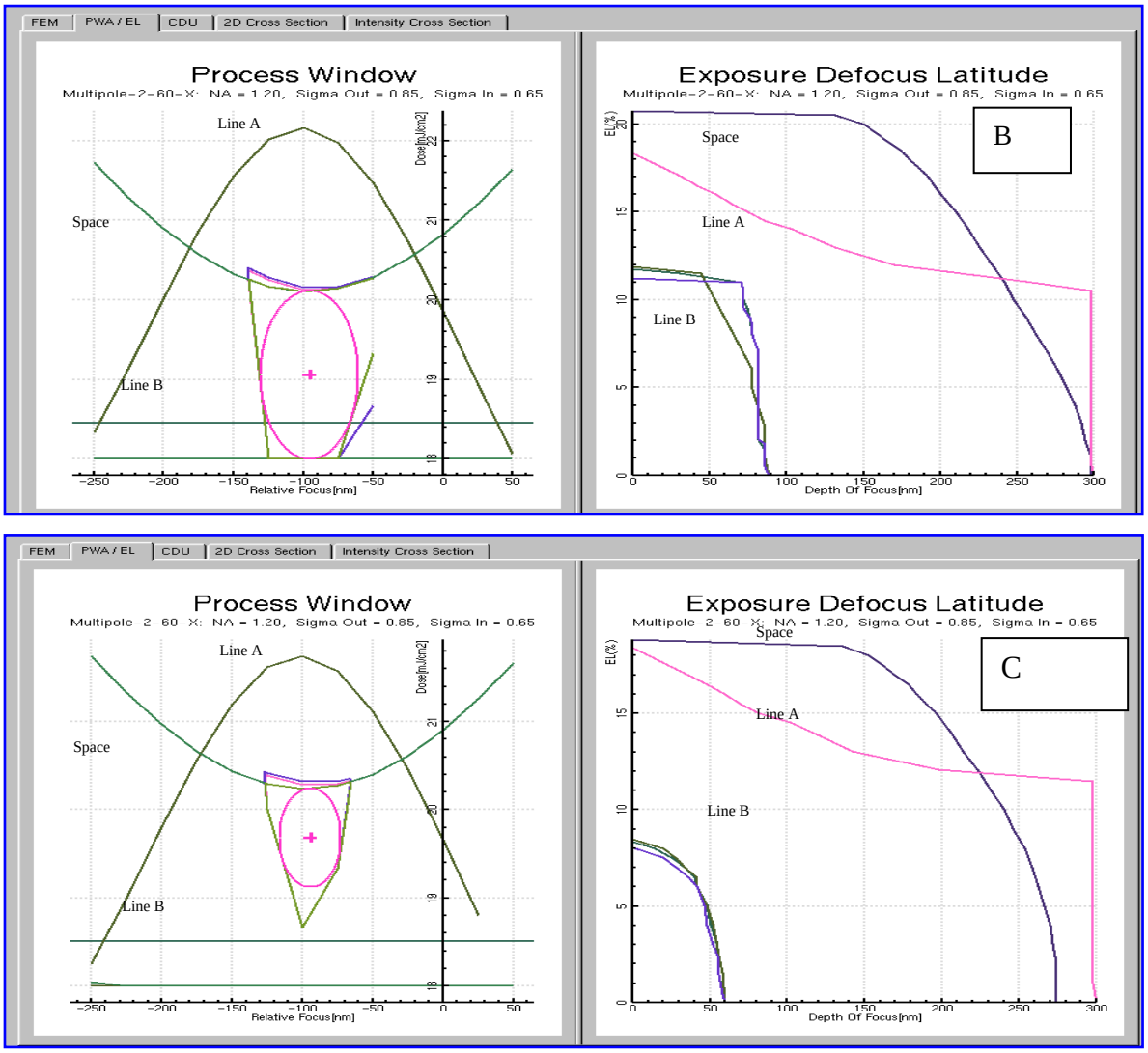

Figure 12: process window plots at different bandwidth settings

3. EXPERIMENTAL RESULTS

3.1 Overlay experiment

In order to confirm the simulations, we ran a 2-pass overlay test, where the first (reference) layer is exposed with the nominal wavelength and the second one with a wavelength set-point offset at two WL offset settings (+0.5pm, -0.5pm) in addition to the baseline exposure. According to the simulations, we expect a maximum effect of about 2.5nm through the slit (see Figure 8) for the most sensitive feature, LINE B. The bandwidth of the laser for this experiment is set to e95=0.25.

Ideally the overlay targets should be representative of standard process monitoring conditions for this technology.

In particular, different types of overlay mark segmentation may exhibit a different sensitivity to chromatic aberrations compared to non-segmented marks. At the same time, the defocus due to longitudinal chromatic aberration may begin to result in contrast loss of segmented marks particularly for higher WL offsets.

The purpose of this test is to extrapolate the shift behavior of different targets with the wavelength in order to convolute the results simulating a bandwidth impact. We will compare the experimental results with the simulations.

3.2 Overlay target and sampling description

The experiment described in the previous section was carried out using Advanced Imaging Metrology (AIM) targets with different features size as reported in Figure 13 a) and measured on Archer™ 100IS metrology tool. Dedicated overlay targets sampling plan was introduced in order to catch distortion map across the field and exposure slit as depicted in Figure 13 b) and c) respectively. Full wafer coverage has been considered.

AIM Targets	Size [µm]	Pitch [µm]	Feature Size [µm]	
			Inner Grating	Outer Grating
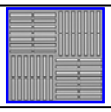	35 x 35	2.4	1.1	1.1
	13 x13	1.2	0.3	0.3
	27 x 27	Optical Grating	0.2	0.2
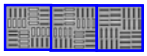 G A E	15x15	1.8	G=1 A=0.7 E=0.4	0.2

a)

b)

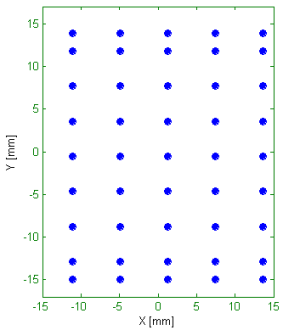

c)

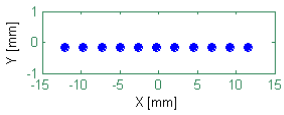

Figure 13: starting from the top: the first 3 rows are AIM targets used for distortion calculation, 2-pass overlay test. The last row shows targets {G, A, E} which are suitable targets to evaluate the imaging fingerprint across the slit. b) Field sampling for 2-pass overlay test. c) Slit sampling for IPE calculation

Except for the {G, A, E} targets, the metrology targets shown in Figure 13 are 2 layers targets where inner and outer gratings of AIM are printed at two different exposure runs. On the contrary, {G, A, E} are single layer AIM targets and printed at the same time in a single exposure run.

In order to have a reliable characterization of metrology measurements we have estimated the maximum error contribution in terms of Total Measurement Uncertainty (TMU) and random error propagation. The result is $3\sigma \leq 0.4$nm. This is the maximum error bar for both X and Y measurements.

3.3 Discussion of the results

The results of metrology measurements, conducted using three different AIM targets as described in the previous section, are presented. As shown later, all measurements using different AIM targets are well matched one to another. Therefore, in Figure 14 only the Non Correctible Errors (NCE) of 13x13 µm AIM targets have been depicted. This match means that the 2-run overlay test is independent from target used for overlay characterization, in particular from feature size of the bar assembling the grating. From Figure 14 , it's clearly visible that both NCE in X and Y are a function of the wavelength shift $\Delta\lambda$. The effects might be ascribed to non-linear overlay contributions. In particular, the NCE Y appears as a 2nd order distortion across the slit whereas the NCE X appears as a 3rd order distortion across the slit,

see Figure 14 b), d) respectively. As is obvious, the reference state $\Delta\lambda=0$ does not have large high order components (however, a small residual 3rd order NCE results from the specific illumination mode used). For what concerns the range of variation in terms of peak to valley (p2v) as a function of wavelength shift with respect to the reference state ($\Delta\lambda=0$), we found p2v of NCE X and NCE Y of around 2nm. From the simulation results we also found errors of around 2nm.

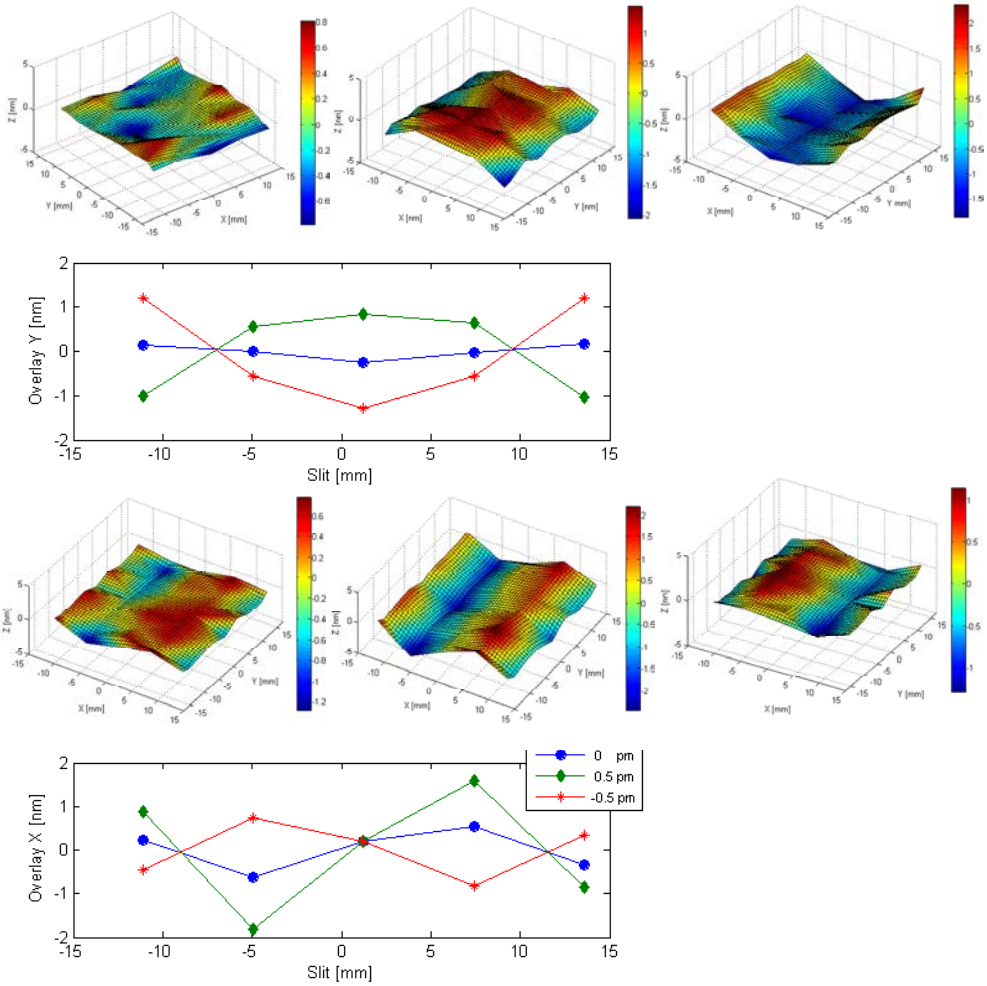

Figure 14: a) NCE in the Y direction across the field and through wavelength shift. b) Orthogonal projection of NCE Y onto the exposure slit. c) NCE X direction across the field and through wavelength d) Orthogonal projection of NCE X onto the exposure slit. The NCE is calculated by subtracting the linear model terms from measured data

3.4 IPE discussion

Considering two different set of variables, wavelength ≡ {$\Delta\lambda=0$, $\Delta\lambda=0.5$, $\Delta\lambda=-0.5$} and IPE targets ≡ {G, A, E} we are able to evaluate the relative maximum contribution to Image Placement Error. Taking a look at Figure 15 and selecting the most sensitive target the relative maximum contribution to IPE as a function of wavelength is ≤ 0.1nm. These experimental results are in good agreement with the simulations shown in Figure 4 for the different product patterns (LINE A, LINE B and SPACE). Keeping the wavelength constant, the relative maximum contribution to IPE as a function metrology targets is ≤ 0.7nm.

As a comparison, a 0.5pm wavelength variation used in these experiments and simulations is over an order of magnitude greater than the laser wavelength stability specification for the XLA 360 generation lasers, and up to two orders of magnitude greater than actual performance for the latest generation XLR lasers.

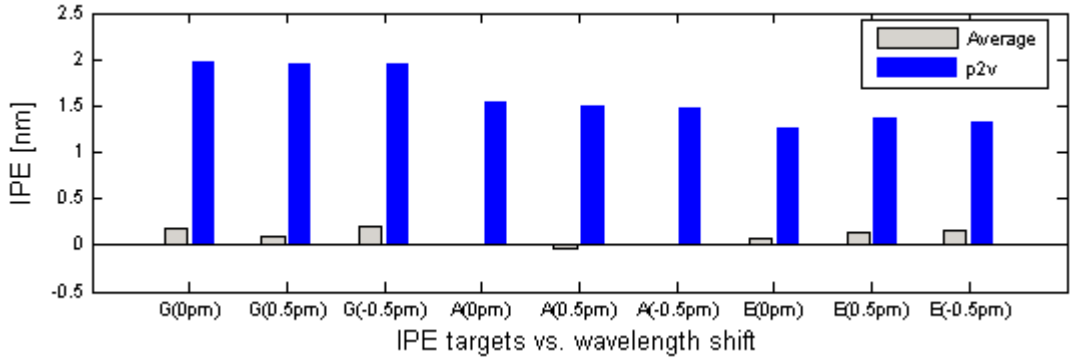

Figure 15: Image Placement Error as a function of metrology targets {G, A, E} and wavelength shift {$\Delta\lambda$=0, $\Delta\lambda$=0.5, $\Delta\lambda$=-0.5}

3.5 IPE simulation with measured Zernikes

To understand the wavelength setpoint effect on overlay we simulate the AIM target shift with the full sets of lens Zernikes collected after each wavelength offset.

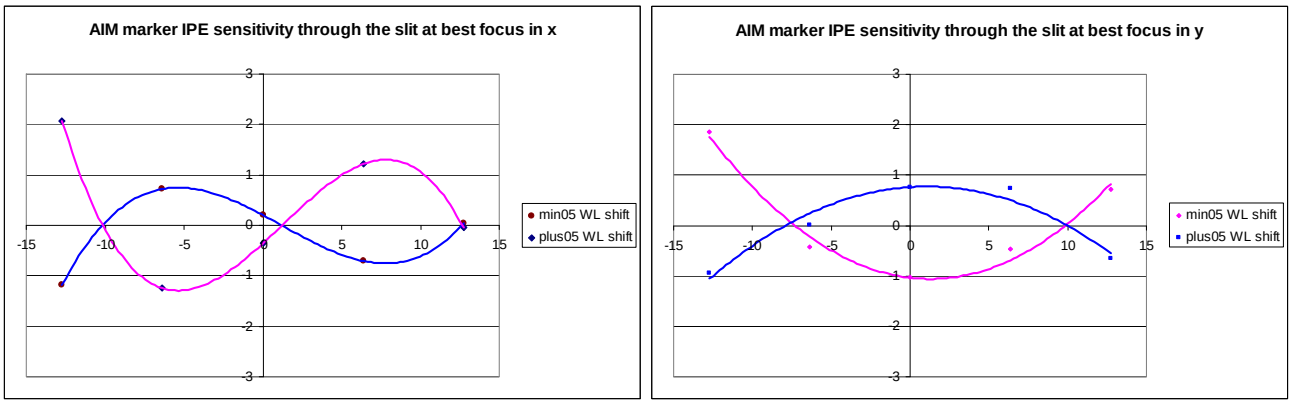

Figure 16: AIM marker IPE sensitivity through the slit

Figure 16 confirms the second order shift in Y and the third order shift in X coming mainly by Z2 and Z3 wavelength sensitivity in the slit.

This effect is not automatically compensated during the exposure inducing a third order in X and second order in Y lens distortion.

These misalignments are anyway perfectly symmetrical with respect to the reference wavelength hence we can conclude that a bandwidth drift considered as a convolution of three wavelengths here analyzed may not significantly impact the lens distortion.

4. SUMMARY AND CONCLUSIONS

The work in this paper has shown the IPE resulting from the higher order Zernike terms are small but depend on the feature type. We simulated the effect and followed up with an experiment to confirm the result.

The maximum across slit IPE that we simulated and subsequently confirmed by an experiment is about 2.5nm, 0.7nm and 0.4nm for the LINE A, LINE B and SPACE features respectively. A simulation found that the effect of a bandwidth variation of 0.5pm is about 0.2 nm to 0.5nm for the most sensitive pattern, LINE B, at the defocus extremes. Note that 0.5pm bandwidth variation modelled in this work is significantly higher than controlled in current-generation lasers.

We found that the DOF of the most sensitive pattern, LINE B, is reduced by about 14% within the standard operating range of the laser. This will be confirmed by an experiment. Current-generation lasers are able to control the bandwidth such that the risk of this type of effect is reduced. The CD Uniformity contribution from the laser to the total CD uniformity budget is estimated by dedicated simulations to be less than 10%.

CDU uniformity as a function of bandwidth depends on the type of pattern and the laser contribution is highest for the LINE A feature. These two results show that asymmetric patterns can be sensitive to bandwidth. We note that the XLR 560i and XLR 660ix both offer lower nominal bandwidth operation and significantly lower bandwidth variability due to bandwidth stabilization technology and a new wavelength controller.

Additionally we showed that the IPE is insensitive to the type of overlay measurement mark. We investigated 3 types of marks and found that the maximum difference is less than 0.1nm. This was also confirmed by a simulation.

An investigation of the 32nm pattern found that it is less sensitive to IPE than the pattern shown in Figure 1.

5. REFERENCES

[1] P. Rigolli et al., "AIM technology for Non-Volatile Memories microelectronics devices", SPIE2006, 6152-175

[2] E. Hendrickx, A. Colina, A. van der Hoff, J. Finders, G. Vandenberghe, Image placement error: closing the gap between overlay and imaging, J. Microlith., Microfab., Microsyst. 4(3), 033006 (Jul–Sep 2005)

[3] P. de Bisschop, I. Lalovic, F. Trintchouk, Impact of finite laser bandwidth on the critical dimension of L/S structures, J. Micro/Nanolith. MEMS MOEMS 7(3), 033001 (Jul–Sep 2008)

[4] M. Smith, J. Bendik, I. Lalovic, N. Farrar, W. Howard, C. Sallee, "Modeling and Performance Metrics for Longitudinal Chromatic Aberrations, Focus-drilling, and Z-noise; Exploring excimer laser pulse-spectra," *Proc. SPIE Optical Microlithography XX* **6520** -127 (2007).

[5] M.Terry, I. Lalovic, G. Wells, A. Smith, Behavior Of Lens Aberrations As A Function Of Wavelength On KrF and ArF Lithography Scanners, Proceedings of SPIE Vol. 4346 (2001)

[6] V.N. Mahajan, Optical Imaging and Aberrations-II: Wave Diffraction Optics, SPIE Press, Bellingham (2001)

[7] I. Lalovic, O. Kritsun, S. McGowan, J. Bendik, M. Smith, N. Farrar, "Defining a physically-accurate laser bandwdith input for optical proximity correction (OPC) and modeling", *Proc. BACUS XXII Photomask Technology Symposium* **7122** -62, (2008).

Laser Produced Plasma Light Source for EUVL

Igor V. Fomenkov*, Alex I. Ershov, William N. Partlo, David W. Myers
Richard L. Sandstrom, Norbert R. Böwering, Georgiy O. Vaschenko, Oleh V. Khodykin, Alexander N. Bykanov, Shailendra N. Srivastava, Imtiaz Ahmad, Chirag Rajyaguru, Daniel J. Golich, Silvia De Dea, Richard R. Hou, Kevin M. O'Brien, Wayne J. Dunstan, David C. Brandt

Cymer Inc., 17075 Thornmint Court, San Diego, CA 92127, USA

ABSTRACT

This paper describes the development of laser-produced-plasma (LPP) extreme-ultraviolet (EUV) source architecture for advanced lithography applications in high volume manufacturing. EUV lithography is expected to succeed 193nm immersion technology for sub-22nm critical layer patterning. In this paper we discuss the most recent results from high EUV power testing and debris mitigation testing on witness samples and normal incidence collectors. Subsystem performance will be shown including the CO2 drive laser, debris mitigation, normal incidence collector and coatings, droplet generation, laser-to-droplet targeting control, intermediate-focus (IF) metrology and system use and experience. In addition, a number of smaller lab-scale experimental systems have also been constructed and tested. This presentation reviews the experimental results obtained on systems with a focus on the topics most critical for an HVM source.

Keywords: EUV source, EUV lithography, Laser Produced Plasma

1. INTRODUCTION

EUV Lithography is the front runner for next generation critical dimension imaging after 193 nm immersion lithography for layer patterning below the 32 nm node; beginning in 2013 according to the International Technology Roadmap for Semiconductors (ITRS). NAND Flash devices are expected to have the need for this manufacturing technology as soon as 2011, with pilot line system introduction starting this year (2010). The availability of high power 13.5 nm sources has been categorized as high risk and ranked as critical with other technologies requiring significant developments to enable the realization of EUV lithography. High sensitivity photoresists with good line-edge-roughness (LER) and line-width-roughness (LWR) are needed to keep the required source power within reasonable limits. Photoresist sensitivity and other light absorbing elements are the basis to derive EUV source power requirements within the usable bandwidth (BW) of 2 %. Scanner manufacturers are requiring clean EUV power close to 200W at the intermediate focus (IF) to enable > 100 wph scanner throughput assuming 10 mJ/cm^2 photoresist sensitivity. The need for a Spectral Purity Filter (SPF) increases the requirements for Raw EUV Power even higher. Clean EUV Power is calculated by taking the Raw EUV power and subtracting the losses associated with the Spectral Purity Filter (SPF) and dose control, for initial sources these losses are estimated to be 35% and 20% respectively. A scalable EUV source architecture is needed to enable the evolution of EUV lithography during the life cycle of the technology. Laser-produced-plasma (LPP) sources are expected to deliver the necessary high power for critical-dimension high-volume manufacturing (HVM) scanners for the production of integrated circuits in the post-193 nm immersion era.[1]

The LT1 source is shown in Figure 1. The ETS has been used since mid 2006 to develop CO_2 laser and tin droplet LPP technology [2]. Many development milestones have been reported from this source and even today it is still being used to test our latest improvements to the overall source architecture. The most recent change was the addition of a fourth amplifier to the CO2 laser to boost the laser power to near 20kW. It operates using the same 30 micron diameter droplets as our production sources. Preformance results of test and prototype sources were discussed in detail

Extreme Ultraviolet (EUV) Lithography, edited by Bruno M. La Fontaine, Proc. of SPIE Vol. 7636, 763639 · © 2010 SPIE · CCC code: 0277-786X/10/$18 · doi: 10.1117/12.848408

previously [3,4,5]. An HVM I source is shown in Figure 2. We have six sources in production with the first three in the final stages of integration and the first one entering test. The HVM I sources use a 5sr normal incidence collector, 30 micron tin droplets and a ~20kW CO_2 laser. The HVM I source is shown in its inclined position of 27 degrees as it is positioned when integrated into the scanner.

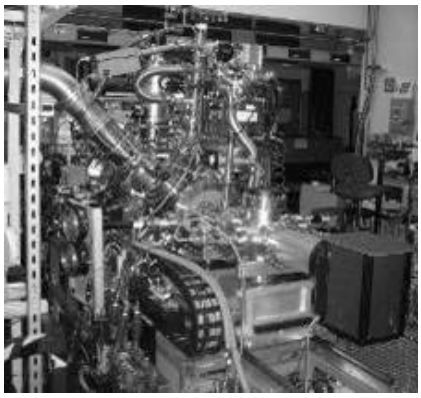

Figure 1: LT1

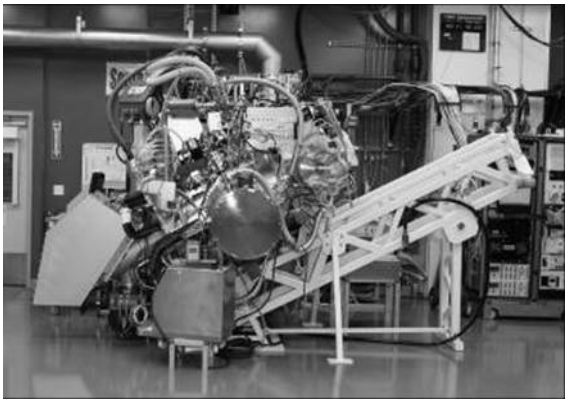

Figure 2: HVM I Source in Production

2. EUV POWER

EUV power technology has been developed on our LT1 source using the same architecture as our production sources but with very flexible designs to allow for rapid prototyping and to apply new learning as fast as possible. The most recent power results are shown in Figure 3 and Figure 4. Both of these results were obtained using 30 micron diameter droplets and a burst duration of 400ms while firing the laser to hit every droplet during the burst. A 10ms sliding window is plotted through the data to show the inherent open loop dose variation. Applying dose control to this level of performance would change the power to the lowest point on this curve, or about 80W.

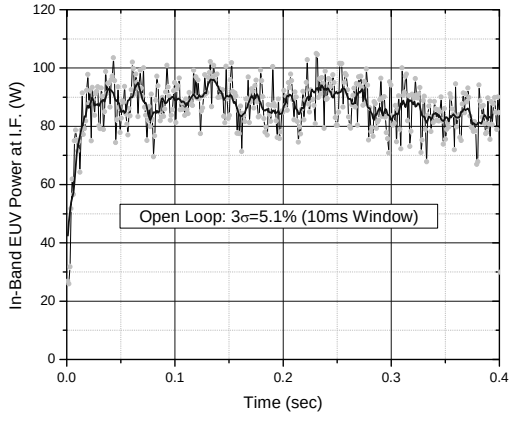

Figure 3: Raw EUV power @ IF at 40% duty cycle

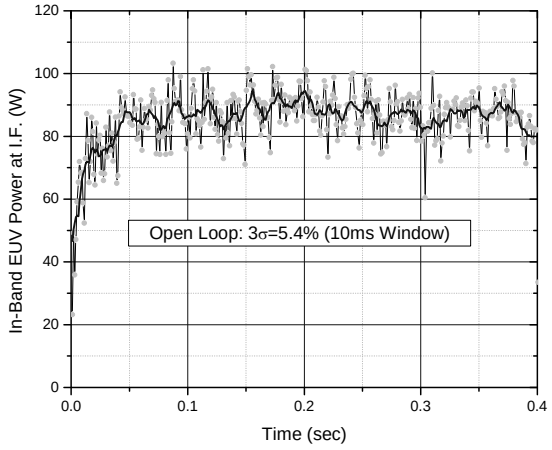

Figure 4: Raw EUV power @ IF at 80% duty cycle

When dose control is applied to the source the stability of the output power meets the requirements set fourth by scanner manufacturers. Figure 5 shows the open loop stability of the EUV output power just before applying the dose control

algorithm, Figure 6 is the stabilized performance during the same run when the algorithm is actively controlling the power output by applying feedback from energy sensors on the source. A dose stability of $3\sigma<\pm 0.35\%$ was achieved.

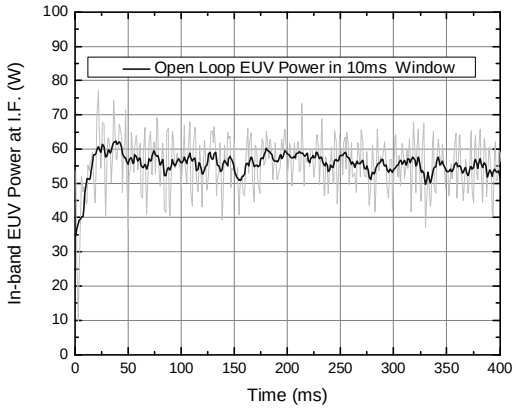

Figure 5: Raw EUV power @ IF at 60% duty cycle

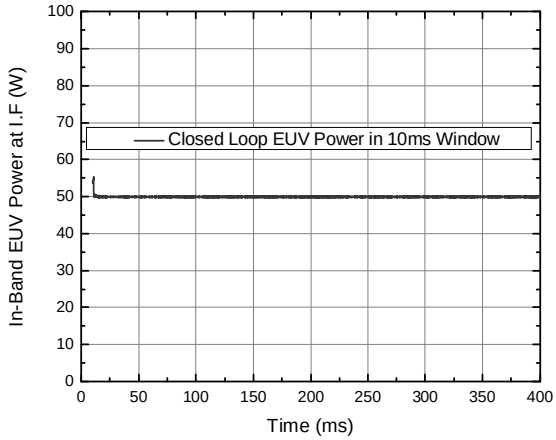

Figure 6: Dose stabilized EUV power @ IF at 60% duty cycle

3. NORMAL INCIDENCE COLLECTORS

Cymer's LPP EUV source employs near-normal-incidence mirrors with a very large solid angle for light collection. Such a geometry has numerous advantages, which has been discussed elsewhere.[6] As we reported earlier[1], the complete infrastructure is in place for manufacturing of large-size normal-incidence collector mirrors. For demonstration of the light collection capabilities of our source several 1.6 sr sub-aperture versions (300 mm optical diameter) have been produced and used in the development system for testing. Several large (> 650 mm diameter) HVM I 5sr collectors are now also completed. The collectors have been coated with graded multilayer coatings with layer periods optimized for high EUV reflectance at the corresponding incidence angles.

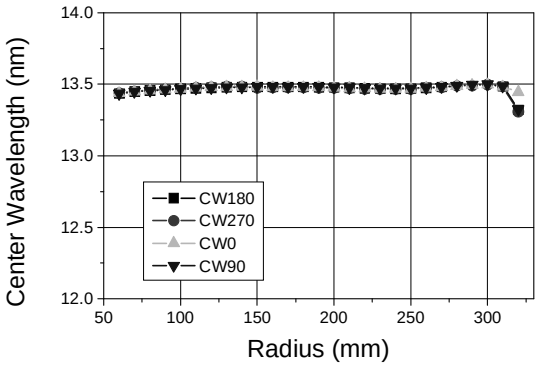

Figure 7: Center wavelength of points measured on four radial lines of a 5sr normal incidence collector mirror after multi-layer coating.

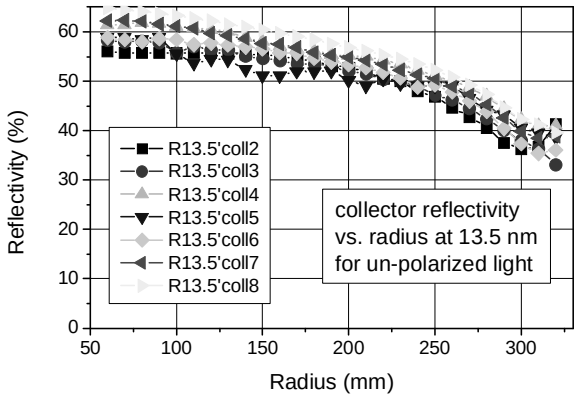

Figure 8: Reflectivity of several 5sr collectors for un-polarized light as a function of mirror radius. The data were determined from measurements with s-polarized EUV light at 13.5nm (PTB) and by scaling according to samples measured with both s-polarized and un-polarized light.

Figure 7 shows the center wavelength of a MLM coated 5sr collector. It is matched well to 13.5 nm wavelength for all radial positions on the mirror. Figure 8 displays the EUV reflectance at 13.5 nm wavelength obtained as a function of radial position for several 5sr mirrors, determined corresponding reflectance values for incidence of unpolarized light as derived from results obtained with test samples at different radial positions. When taking into account the contributing reflecting area, the reflectance for unpolarized light at 13.5 nm corresponds to an average value of >50 %.

4. DROPLET GENERATOR

The droplet generator provides a constant stream of liquid tin targets (droplets) to the focal point of the collector where the CO_2 laser pulse is used to create the light-emitting plasma. The main requirement for the generators is to produce reproducibly small droplet targets of identical size at the repetition rate of the laser pulses (typically 50 kHz) [7] Droplets with high temporal and spatial stability have been consistently produced over hundreds of hours of operation time, with the duration mainly limited by the capacity of the tin reservoir vessel. The longest continuous run of the droplet generator achieved so far is in excess of 500 hours. Figure 9 shows the position stability of 16 μm diameter droplets when the stream is propagating in a horizontal direction. Short-term position stability is better than 1 μm. The slow position drift can be compensated by the active position control system as was demonstrated separately.

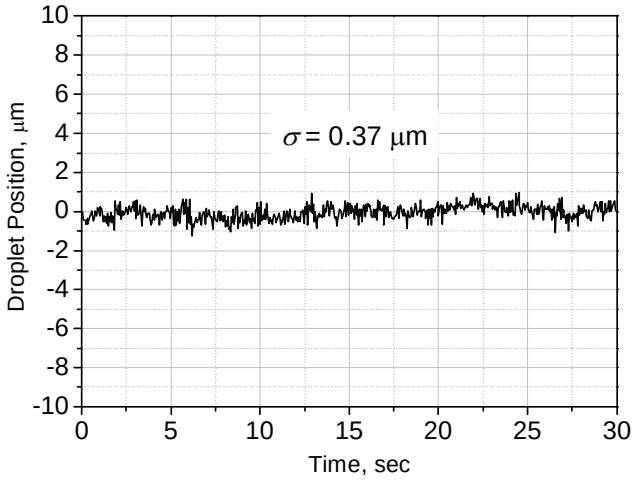

Figure 9: Position stability of 16 μm droplets.

We have developed the technology for generating droplets with diameter of ~16 μm. These droplets meet the stability and timing requirements for the present system, as was tested during 200 hours of operation without failure. Droplet size reduction leads to a significant efficiency increase for debris mitigation technologies. Second generation sources should have droplet diameters further reduced to these sizes. When droplets of this size are generated at a frequency of 50 kHz, about 1 liter of tin is consumed per year.

5. DEBRIS MITIGATION

Our debris mitigation system works by the use of hydrogen buffer gas to stop high energy fast ions and to remove tin deposition at a rate faster than it is deposited, or zero net deposition. Hydrogen buffer gas ability to stop tin ions has been described previously [3], and is shown in Figure 10. As the buffer gas pressure is increased both the ion energy and ion flux reaching the surface of the collector is reduced significantly. This technique has been previously shown to keep witness samples free of ion erosion and tin deposition[3].

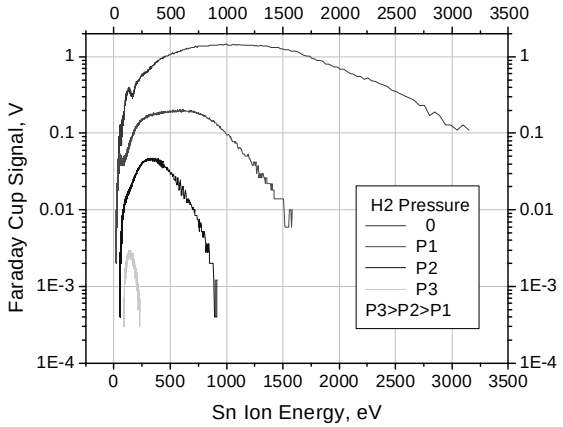

Figure 10: Hydrogen buffer gas pressure vs. ion energy and flux at the location of the collector surface

Hydrogen buffer gas debris mitigation was tested on a 5 sr collector in a prototype source that was subsequently shipped to a leading scanner manufacturer. The 5 sr collector was kept free of both erosion and deposition over a 9 hour period or about 600 million pulses[5]. The test was performed on 30 micron diameter droplets using 400ms burst duration at 40% duty cycle and EUV output power of ~15W at IF. Figure 11 shows a far field image of the EUV distribution and collector reflectivity after 2 hours. These images were taken with a fluorescence converter and CCD camera behind IF. Figure 12 shows the same collector after 9 hours of exposure with no change to the image quality.

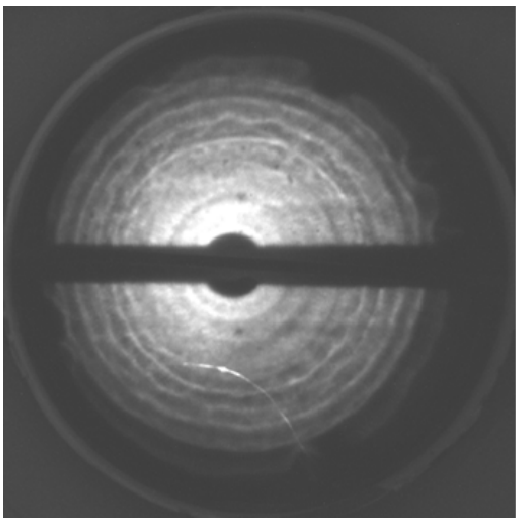

Figure 11: Far field image of EUV distribution and collector reflectivity after 2 hours of exposure

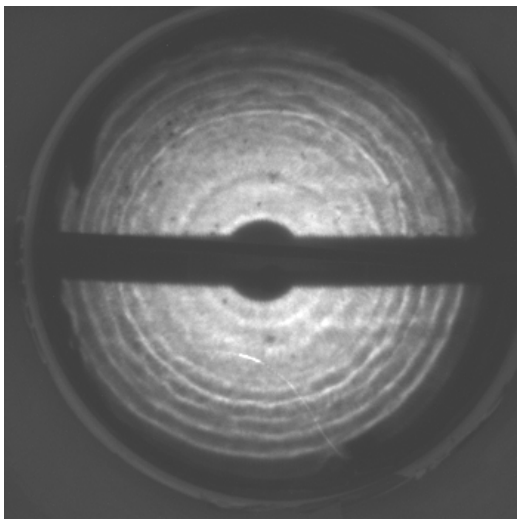

Figure 12: Far field image of EUV distribution and collector reflectivity after 9 hours of exposure

6. SUMMARY

Laser-produced plasma has been shown to be the leading source technology with scalability to meet requirements from leading scanner manufacturers and provide a path toward higher power as the lithography tools evolve over their life cycle. EUV power exceeding 90W at intermediate focus at 80% duty cycle and 400ms burst length has been reported. Normal-incidence collector mirrors of diameter > 650mm, with > 5 sr light collection and average reflectivities >50%

are produced and integrated into production LPP systems. LPP EUV source system manufacturing has progressed well. The high-conversion-efficiency combination of 10.6 μm laser radiation and Sn source element has been demonstrated with CE in excess of 3 %. EUV lithography is expected to be the critical dimension imaging solution in the post-193 nm immersion era. LPP source technology with power levels exceeding 400W is expected to enable the IF power requirement projected in the future, and to provide the much needed margin for photoresist sensitivity, spectral purity filters, optics degradation, process latitude, and overall equipment throughput. Cymer plans the commercialization of EUV light sources in 2010. The company continues to meet its EUV source development commitments to industry, customers and suppliers.

ACKNOWLEDGEMENTS

The authors gratefully acknowledge the valuable contributions from Martin J. Neumann and David N. Ruzic of University of Illinois, Urbana Champaign, Marco Perske, Hagen Pauer, Mark Schürmann, Sergiy Yulin, Torsten Feigl and Norbert Kaiser of Fraunhofer Institut f. Angewandte Optik und Feinmechanik, Eric Gullikson and Farhad Salmassi of Lawrence Berkeley National Laboratory, Frank Scholze, Christian Laubis, Christian Buchholz and coworkers at PTB, and Mark Tillack and Yezheng Tao of the University of California at San Diego. We are also very thankful for the invaluable support and contributions, past and present, of many scientists, engineers and technicians involved in the EUV technology program at Cymer.

REFERENCES

[1] I. V. Fomenkov, D. C. Brandt, A. N. Bykanov, A. I. Ershov, W. N. Partlo, D. W. Myers, N. R. Böwering, G. O. Vaschenko, O. V. Khodykin, J. R. Hoffman, E. Vargas L., R. D. Simmons, J. A. Chavez, C. P. Chrobak, in: *Proc. of SPIE Vol. **6517**, Emerging Lithographic Technologies XI*, M. J. Lercel, ED., 65173J (2007).

[2] D. C. Brandt, I. V. Fomenkov,, A. I. Ershov, W. N. Partlo, D. W. Myers, N. R. Böwering, A. N. Bykanov, G. O. Vaschenko, O. V. Khodykin, J. R. Hoffmann, E. Vargas L., R. D. Simmons, J. A. Chavez, C. P. Chrobak, in: *Proc. of SPIE Vol. **6517**, Emerging Lithographic Technologies XI,* M. J. Lercel, ED., 65170Q (2007).

[3] D. C. Brandt, I. V. Fomenkov, A. I. Ershov, W. N. Partlo, D. W. Myers, N. R. Böwering, N. R. Farrar, G. O. Vaschenko,O. V. Khodykin, A. N. Bykanov, J. R. Hoffman, C. P. Chrobak, S. N. Srivastava, I. Ahmad, C. Rajyaguru, D.J. Golich, D. A. Vidusek, S. De Dea, R. R. Hou, in: *Proc. of SPIE Vol. **7271**, Alternative Lithographic Technologies*, F. M. Schellenberg, B. M. La Fontaine, Eds., 727103, (2009).

[4] I. V. Fomenkov, D. C. Brandt, A. N. Bykanov, A. I. Ershov, W. N. Partlo, D. W. Myers, N. R. Böwering, N. R. Farrar, G. O. Vaschenko, O. V. Khodykin, J. R. Hoffman, C. P. Chrobak, S. N. Srivastava, D.J. Golich, D. A. Vidusek, S. De Dea, R. R. Hou, in: *Proc. of SPIE Vol. **7271**, Alternative Lithographic Technologies*, F. M. Schellenberg, B. M. La Fontaine, Eds., 727138 (2009).

[5] N. R. Böwering, I. V. Fomenkov, D. C. Brandt, A. N. Bykanov, A. I. Ershov, W. N. Partlo, D. W. Myers, N. R. Farrar, G. O. Vaschenko, O. V. Khodykin, J. R. Hoffman, C. P. Chrobak, S. N. Srivastava, I. Ahmad, C. Rajyaguru, D.J. Golich, D. A. Vidusek, S. De Dea, R. R. Hou, Journal of Micro/Nanolith. MEMS MOEMS 8(4), 041504 (2009).

[6] N. R. Böwering, A. I. Ershov, W. F. Marx, O. V. Khodykin, B. A. M. Hansson, W. N. Partlo, E. Vargas L., J. A. Chavez, I. V. Fomenkov, D. W. Myers, D. C. Brandt, in: *Proc. of SPIE Vol. **6151**, Emerging Lithographic Technologies X*, M. J. Lercel, Ed., 61513R (2006).

[7] J. M. Algots, O. Hemberg, A. Bykanov, in: *Proc. of SPIE Vol. **5751**, Emerging Lithographic Technologies IX*, R. S. Mackay, Ed., 248-259 (2005).

Laser Spectrum Requirements for Tight CD Control at Advanced Logic Technology Nodes

R. C. Peng*[a], H. J. Lee[a], John Lin[a], Arthur Lin[b], Allen Chang[c], and Benjamin Szu-Min Lin[c]
[a]MTC, Taiwan Semiconductor Manufacturing Corp., Hsinchu Science Park, Hsinchu, Taiwan 300-77, R.O.C.; [b]KLA-Tencor Corp., Chupei City, Hsinchu, Taiwan, R.O.C.; [b]Cymer Inc., Kuang Fu Rd. HsinChu, Taiwan, R.O.C.

ABSTRACT

Tight circuit CD control in a photolithographic process has become increasingly critical particularly for advanced process nodes below 32nm, not only because of its impact on device performance but also because the CD control requirements are approaching the limits of measurement capability. Process stability relies on tight control of every factor which may impact the photolithographic performance. The variation of circuit CD depends on many factors, for example, CD uniformity on reticles, focus and dose errors, lens aberrations, partial coherence variation, photoresist performance and changes in laser spectrum. Laser bandwidth and illumination partial coherence are two significant contributors to the proximity CD portion of the scanner CD budget. It has been reported that bandwidth can contribute to as much as 9% of the available CD budget, which is equivalent to ~0.5nm at the 32nm node. In this paper, we are going to focus on the contributions of key laser parameters e.g. spectral shape and bandwidth, on circuit CD variation for an advanced node logic device. These key laser parameters will be input into the photolithography simulator, Prolith, to calculate their impacts on circuit CD variation. Stable though-pitch proximity behavior is one of the critical topics for foundry products, and will also be described in the paper.

Keywords: CD control, laser parameter, laser spectrum, photolithography simulation

1. INTRODUCTION

As critical dimension (CD) is shrunk following Moore's Law, tight circuit CD control becomes more and more difficult, because of not only the reduced CD tolerance, but also hitting the equipment control limitations and CD measurement limitations. There are many factors that impact CD variations, for example, CD uniformity on reticles, focus errors, lens aberrations, partial coherence variation, photoresist performance and laser spectrum. Laser bandwidth and illumination partial coherence are two of the largest contributors to the proximity CD portion of the scanner CD budget, in the other words, Iso-Dense Bias (IDB) or through-pitch performance. IDB performance can be attributed to numerous factors that generate changes in image contrast or induce focus blur, for examples, illumination condition adjustment and laser light source spectral bandwidth (E95%). These factors are necessary to be controlled to fully compensate for IDB variation to the level required at advanced process nodes.[1]-[5]

In previous studies, the sensitivity of IDB and through-pitch performance with regards to laser spectral bandwidth were reported for both 45nm Node logic device[6] and 32nm Node logic device.[7] These results showed that for IDB change of 1nm, E95% variation needs to be controlled to 69fm and 45fm, for 45nm and 32nm logic devices respectively. Increasingly higher spectral bandwidth stability is required for each successive technology node. This indicates that the 22nm Node will demand even tighter bandwidth stability and the added ability to set spectral bandwidth with both high accuracy and flexibility.

Factors from light sources impacting product yields can be divided into two groups, CD control and overlay. Figure 1 shows the laser parameters that contribute to CD control and overlay. Contrast and intensity are two key factors that impact CD control. With further breaking down, the key laser parameters contributing CD control are bandwidth, spectral shape, ASE, wavelength stability, beam stability, energy stability, laser coherence and polarization. In this manuscript, the effects of laser parameters, specifically bandwidth and spectral shape, on CD control will be discussed.

Optical Microlithography XXIII, edited by Mircea V. Dusa, Will Conley, Proc. of SPIE Vol. 7640, 76402C · © 2010 SPIE · CCC code: 0277-786X/10/$18 · doi: 10.1117/12.846516

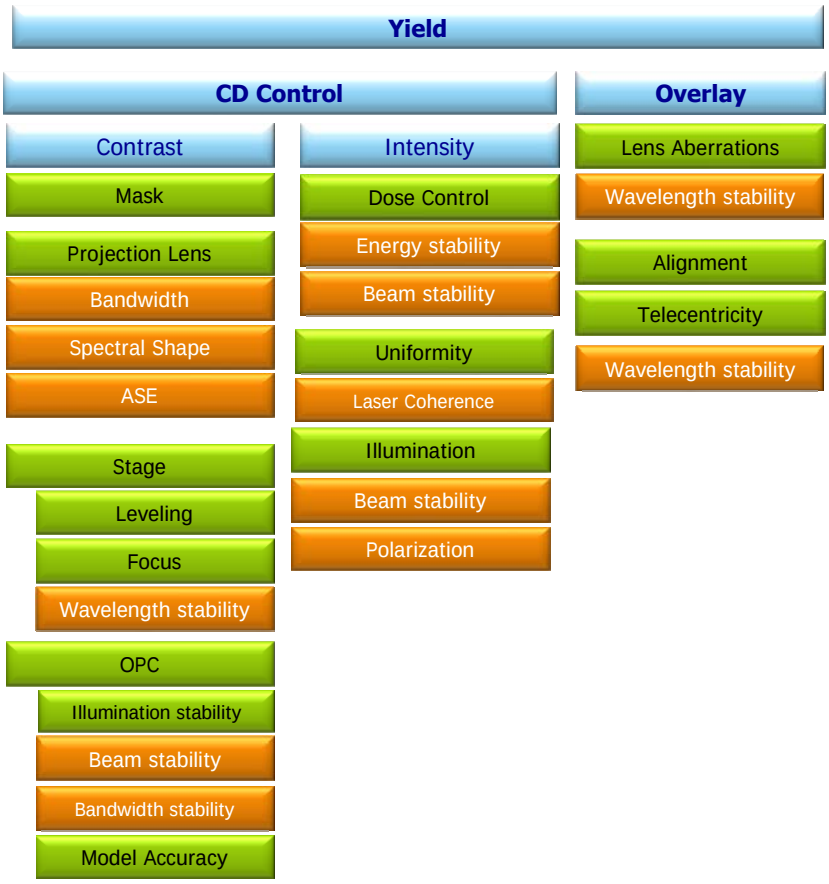

Figure 1. The key laser parameters contributing to product yield (CD control + overlay).

2. SIMULATION CONDITIONS

Figure 2 illustrates the flow chart used for simulation. An L/S layer from an advanced node logic device was chosen as the target layout for this simulation work. Through-pitch 1-D L/S patterns from the minimum pitch to full isolated features were simulated. No sub-resolution assistant features (SRAFs) were used, but only mask biases were applied to compensate the optical proximity effects at a certain chosen laser condition. Original through-pitch 1-D L/S patterns and illumination conditions (193nm Immersion + Dipole illumination + Y-Polarization + Att. PSM) were the 1st set of input parameters to calculate the Eop to meet the nominal target CD size for the feature with the minimum pitch and then calculate mask biases for all the other features. Prolith version Ver. X3 was used for all the simulation work in this manuscript. Only aerial image CDs were taken into account for simplifying the simulation work. Varied laser parameters, including E95, were used as the 2nd set of input parameters to check through-pitch DOF (@ 5% exposure latitude), proximity CDs, and CDU. Sigma fine-tuning was the 3rd set of input parameters to improve DOF at the forbidden pitches; optimum center sigma and radius sigma values were selected to achieve enough process margins for those forbidden pitches. Laser requirements were then derived from simulated CD results, and E95 CD sensitivity to meet the target CD/CDU criteria.

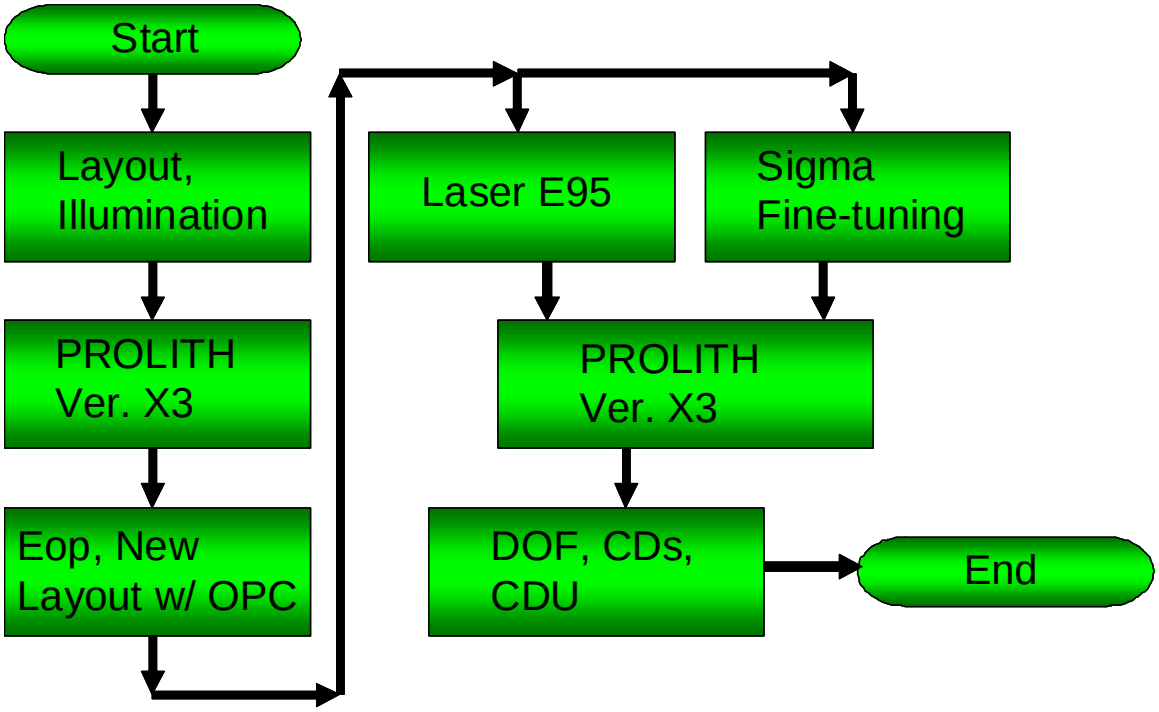

Figure 2. Simulation Flow Chart.

3. RESULTS AND DISCUSSIONS

3.1 DOF and CDU

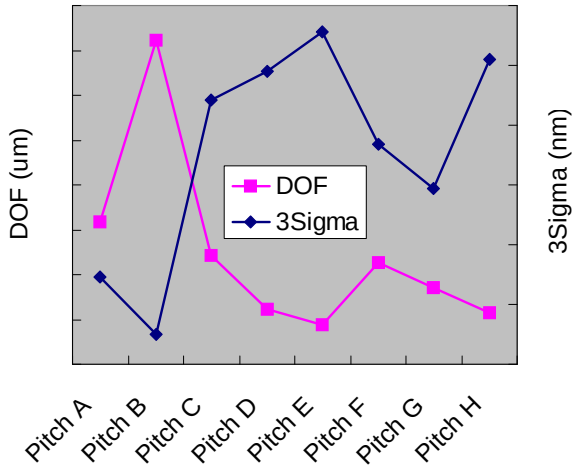

Figure 3. The through-pitch simulation results of DOF and CDU with assigned illumination conditions and built-in Cymer XLA light source parameters. The square line represents the through-pitch DOF trend while the diamond line the through-pitch CDU trend.

Figure 3 illustrates the through-pitch simulation results of DOF and CDU with assigned illumination conditions and built-in Cymer XLA300 light source parameters. The square line represents the through-pitch DOF trend while the diamond line the through-pitch CDU trend. No SRAFs were added but optimal mask biases were applied to through-pitch 1-D L/S patterns to compensate the OPC effects. Dipole illumination enhances the DOF and CDU values at the tighter pitches, however, the forbidden pitches (Pitch D and E) and isolated (Pitch H) L/S features show less DOF and expectedly worse CDU. It was believed that SRAFs could definitely enhance DOF and CDU for those isolated features, but would not improve DOF and CDU for the forbidden-pitch features because of insufficient space to insert any SRAF, under the reticle manufacturability constraints. Under the current illumination conditions and process settings, CD variations at forbidden pitches should be considered as the worst cases instead of CD behaviors at isolated features as usual due to their narrower process margins.

3.2 Bandwidth CD Dependency

Figure 4 shows the proximity curves in terms of CD differences exposed at different Cymer XLA laser bandwidths. E95%, instead of FWHM (full-width-half-maximum, default tunable parameter in Prolith Ver. X3), was used to represent the laser bandwidth changes here. The simulated E95% range in this study is from 355fm to 555fm. Proximity CD difference curve at an E95% of 435fm is flat because the through-pitch optimal mask biases were calculated at this condition. Based on the same mask bias settings, proximity CD difference curves for different E95% values were then calculated. Larger proximity CD difference variations occur as E95% is changed for the forbidden-pitches (Pitch D and E) and isolated (Pitch H) patterns. Even without SRAF, the proximity CD difference variation as a function of E95% at Pitch E is higher than that at isolated patterns. This indicates that forbidden-dense bias (FDB) may be a more relevant measure of bandwidth sensitivity than isolated-dense bias (IDB).

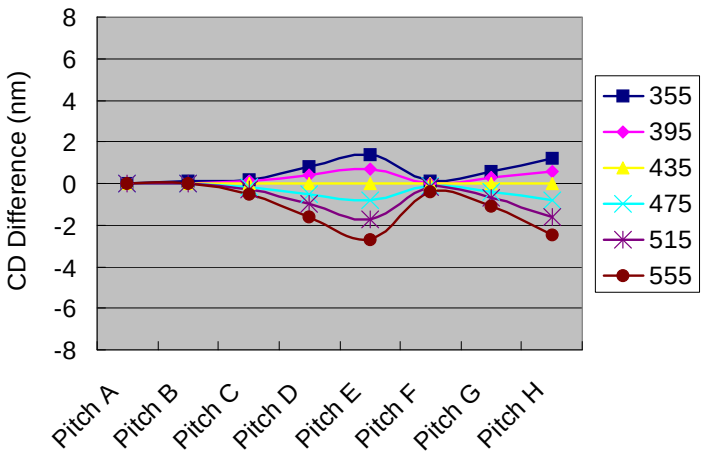

Figure 4. The proximity curves in terms of CD differences exposed at different Cymer XLA laser bandwidths. E95%, ranged from 355fm to 555fm, instead of FWHM (full-width-half-maximum, default tuning parameter in Prolith Ver. X3) and was used to indicate the laser bandwidth here. Proximity CD difference curve under E95% of 435fm is flat because the through-pitch optimal mask biases was calculated at this condition.

The E95% CD sensitivities of different pitches in the E95% range from 355fm to 555fm were calculated in Figure 5. The range of E95% - CD sensitivities is from 0.23nm/100fm to 2.04nm/100fm. The CD variation is derived as 0.09nm ~ 0.81nm based on typical Cymer XLA performance resulting in E95% 3 sigma of 40fm without active bandwidth control. In this case, CD variation can be improved down to 0.05nm ~ 0.47nm by Cymer new XLR platform, which features advanced bandwidth stabilization (ABS) technology, with typical long term E95% stability of 3 sigma of 23fm as shown in Figure 6. Pitch C and Pitch F patterns have the lowest E95% CD sensitivities of 0.35nm/100fm and 0.23nm/100fm, respectively. The highest E95% CD sensitivity occurs at forbidden pitch (Pitch E), while the 2nd highest E95% CD sensitivity occurs for isolated (Pitch H) patterns. If SRAF can be optimally implemented for isolated patterns and use of patterns with forbidden pitch (Pitch E) is restricted, the maximum E95% CD sensitivity can be improved by 42% (from

2.04nm/100fm to 1.19nm/100fm), which means 0.27nm CD variation under typical performance of Cymer's XLR platform long term stability of 23 fm E95%.

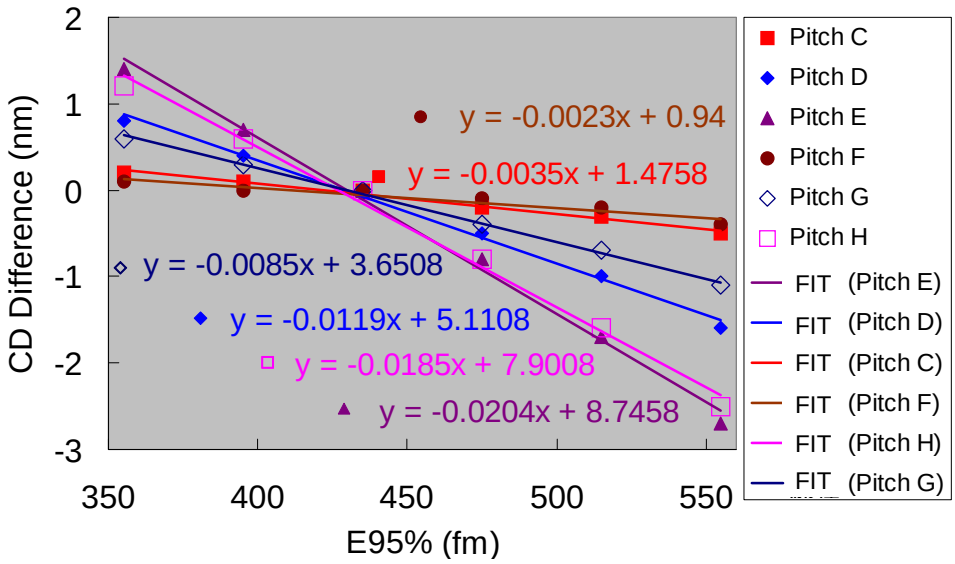

Figure 5. The E95% CD sensitivities of different pitches in the E95% range from 355fm to 555fm were calculated. The range of E95% CD sensitivities are from 0.23nm/100fm to 2.04nm/100fm.

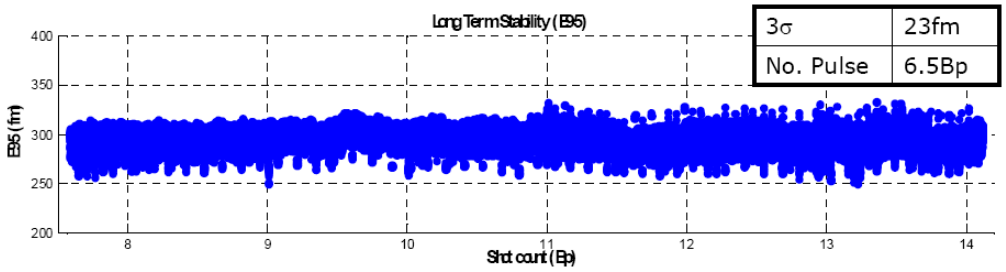

Figure 6. Typical long term E95% stability (3 sigma of 23fm) of Cymer new XLR platform with pulse numbers over 6 Bp. CD variation can be further improved as 0.05nm ~ 0.47nm by this Cymer new XLR platform.

Spectral Shape Effects

Besides Cymer XLA300 spectrum as a built-in light source spectrum in Prolith for accurate simulation, a Lorentzian spectrum is also available for parametric and fast simulation. However, Lorentzian spectral shape looks very different from the Cymer XLA300 spectral shape. Power law coefficient (PLC) in Prolith Ver. X3 is therefore created to vary the Lorentzian spectral shapes into what is referred to as modified Lorentzian. Figure 7 demonstrates the spectral shapes of (a) Lorentzian spectral shape with PLC=1, (b) Lorentzian spectral shape with PLC=2, and (c) Cymer XLA300 spectral shape. It is obvious that the peak of the modified Lorentzian shape becomes rounded and the tails are suppressed as PLC increases from 1 to 2, which result in the modified Lorentzian spectral shape more closely fitting the Cymer XLA300 spectral shape. The effects of using the modified Lorentzian or Gaussian analytic approximations to actual laser spectra were also discussed previously.[8]

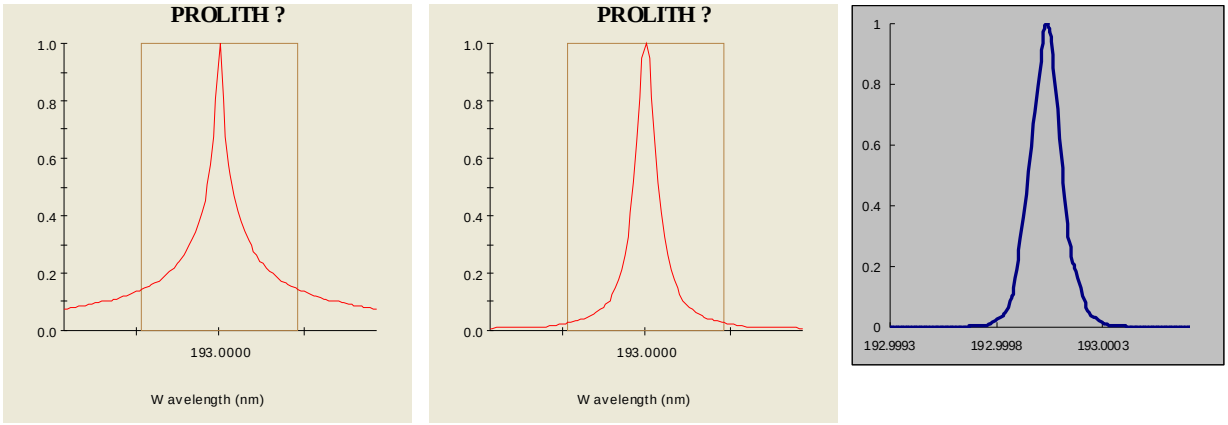

(a) (b) (c)

Figure 7. The spectral shapes of (a) Lorentzian spectral shape with PLC=1, (b) Lorentzian spectral shape with PLC=2, and (c) Cymer XLA300 spectral shape.

The proximity curves, in terms of their CD differences, can be drawn in Figure 8(a) and Figure 8(b) with Lorentzian spectral shape with PLC=1 and Lorentzian spectral shape with PLC=2, respectively. CD differences of the case of PLC=1 is apparently higher than that of the case of Cymer XLA300, while CD differences of the case of PLC=2 much closer to the case of Cymer XLA300. Even though, bandwidth CD sensitivity of the case of PLC=2 is calculated as 2.8nm/100fm, which is about 40% larger than bandwidth CD sensitivity of Cymer XLA300 as 2.04nm/100fm.

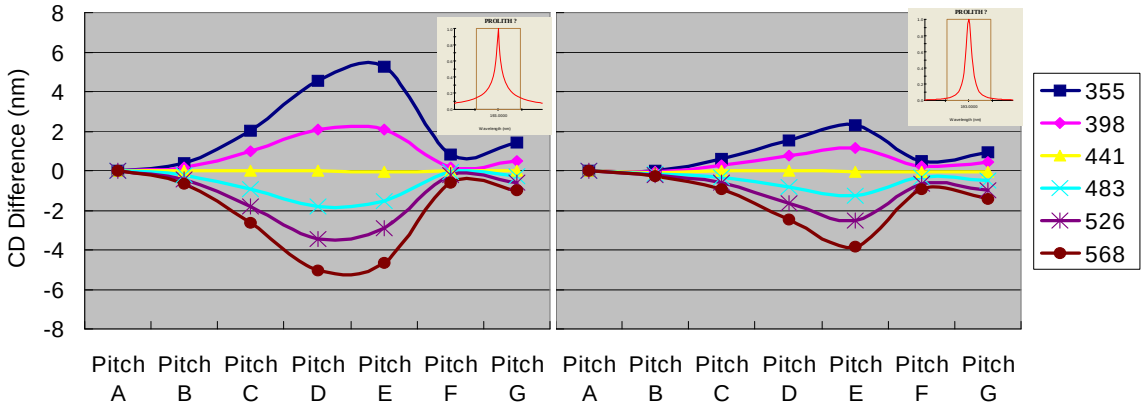

(a) (b)

Figure 8. The proximity curves in terms of CD differences with (a) Lorentzian spectral shape with PLC=1 and (b) Lorentzian spectral shape with PLC=2.

In order to matching modified Lorentzian spectral shapes and actual Cymer XLA300 spectral shape more closely, modified Lorentzian spectra with higher PLCs were studied. From the log scale overlapping spectral chart (Figure 9), it can be told that modified Lorentzian spectral shape with PLC=4 matches actual Cymer XLA spectral shape, except those low level noises at the actual spectral footings.

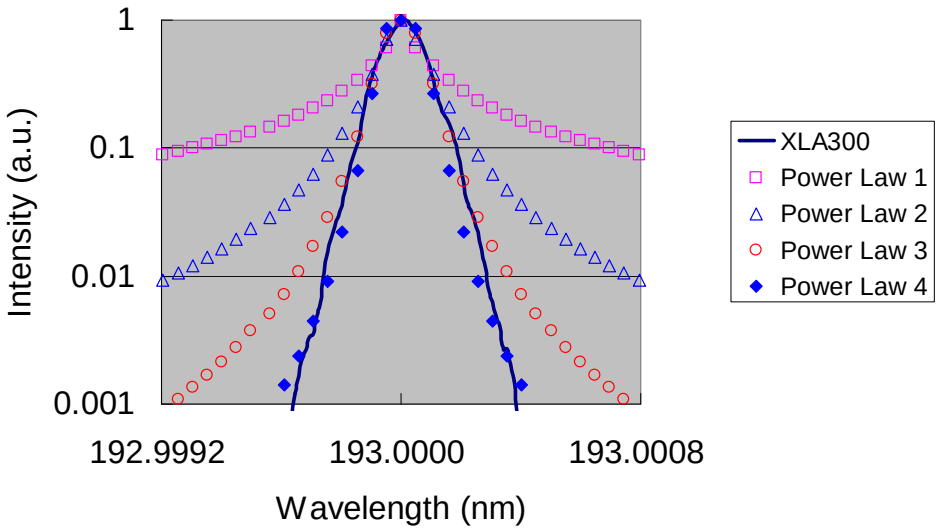

Figure 9. Lorentzian spectral shapes with PLC from 1 to 4 overlapped with actual Cymer XLA300 spectral shape.

Illumination Optimization

Illumination optimization is a common and well-known way to improve DOF and CD variation of the forbidden-pitch patterns. However, it will suffer the process margin loss for those patterns with tighter pitches. Table 1 shows the relative DOF values (100% DOF @ Pitch E pattern under dipole center of 0.9 and dipole radius of 0.05) at different dipole center sigma and radius sigma combinations for Pitch A and Pitch E patterns. Dipole illumination generally favors tighter pitches and any off-optimal condition will result in a reduction of dense pattern process margins. Table 1(a) shows relative DOF values for Pitch A patterns, and the maximum DOF value occurs at the condition of dipole center of 0.8 and dipole radius of 0.05. Although DOF for Pitch E patterns, shown in Table 1(b), also achieves the maximum value under the Pitch A preferred condition, it may soon drop to zero if dipole center or dipole radius shifts to a lower value. In order to improve the process control margins, suggested dipole conditions could be (1) dipole center of 0.85 and dipole radius of 0.1 and (2) dipole center of 0.85 and dipole radius of 0.05, depending on the controllability of dipole center and dipole radius.

DOF	Dipole Radius Sigma			
Dipole Center Sigma	0.05	0.1	0.15	0.2
0.6	133%	170%	146%	212%
0.65	201%	211%	272%	399%
0.7	323%	373%	497%	505%
0.75	836%	972%	715%	507%
0.8	1596%	943%	684%	485%
0.85	632%	845%	671%	520%
0.9	266%	296%	439%	515%

(a)

DOF	Dipole Radius Sigma			
Dipole Center Sigma	0.05	0.1	0.15	0.2
0.6	0%	0%	0%	127%
0.65	0%	0%	0%	0%
0.7	0%	0%	0%	0%
0.75	0%	0%	0%	0%
0.8	204%	0%	0%	0%
0.85	145%	153%	154%	0%
0.9	100%	119%	126%	135%

(b)

Table 1. The relative DOF values (100% DOF @ Pitch E pattern under dipole center of 0.9 and dipole radius of 0.05) at different dipole center sigma and radius sigma combination for (a) Pitch A and (b) Pitch E patterns.

4. CONCLUSION

In this manuscript, key laser light source parameters, e.g. bandwidth and spectral shape, have been studied to determine their contributions to CD variation and proximity variation. E95% forbidden-dense bias (FDB) should be characterized in addition to the usual IDB, because FDB has a higher E95% CD sensitivity due to the narrower process margins. Bandwidth dependent CD variation of 0.47nm for the advanced node logic device can be achieved with typical Cymer XLR long term E95% bandwidth performance of 3 sigma of 23fm, which is enabled by advanced bandwidth stabilization and control technologies. Bandwidth dependent CD variation can be further improved down to 0.27nm by adding SRAFs to isolated patterns and avoiding the use of the forbidden pitch (Pitch E in this case) in the pattern design. Illumination optimization can also increase DOF for those forbidden-pitch patterns, which can also improve E95% FBD sensitivity. In this study, we find that the Modified Lorentzian spectrum with PLC=4 can match the imaging results obtained using a Cymer XLA300 spectral shape at best focus.

REFERENCE

[1] M. Terry et al., "*Behavior of lens aberrations as a function of wavelength on KrF and ArF lithography scanners*", Optical Microlithography XIV, SPIE 4346-41 p.15-24 (2001).

[2] T. Brunner et al., "*Laser bandwidth and other sources of focus blur in lithography*", Optical Microlithography XIX, SPIE 6154-31 (2006).

[3] Kevin Huggins et al., "*Effects of laser bandwidth on OPE in a modern lithography tool*", Optical Microlithography XIX, SPIE 6154-36 (2006).

[4] Feder Trintchouk et al., "*XLA 300: the Forth-Generation ArF MOPA Light Source for Immersion Lithography*", Optical Microlithography XIX, SPIE 6154-76 (2006).

[5] T. Oga et al., "*Challenging to meet 1nm Iso- Dense Bias (IDB) by controlling Laser Spectrum*", Advanced

Lithography XXI, SPIE 6520-144 (2007).

[6] K. Yoshimochi et al., "*45nm Node Logic Device OPE Matching between Exposure Tools Through Laser Bandwidth Tuning*", Optical Microlithography XXI, SPIE 6924-92 (2008).

[7] K. Yoshimochi et al., "*32nm Node Device Laser-bandwidth OPE Sensitivity and Process Matching*", Optical Microlithography XXI, SPIE 7274-115 (2009).

[8] Lalovic et al., "*Defining a physically-accurate laser bandwidth input for optical proximity correction (OPC) and modeling*", Proc. BACUS XXII Photomask Technology Symposium 7122-62, (2008).

Lithography Light Source Fault Detection

Matthew Graham, Erica Pantel, Patrick Nelissen, Jeffrey Moen, Eduard Tincu,
Wayne Dunstan, Daniel Brown
Cymer Inc.

ABSTRACT

High productivity is a key requirement for today's advanced lithography exposure tools. Achieving targets for wafers per day output requires consistently high throughput and availability. One of the keys to high availability is minimizing unscheduled downtime of the litho cell, including the scanner, track and light source. From the earliest eximer laser light sources, Cymer has collected extensive performance data during operation of the source, and this data has been used to identify the root causes of downtime and failures on the system. Recently, new techniques have been developed for more extensive analysis of this data to characterize the onset of typical end-of-life behavior of components within the light source and allow greater predictive capability for identifying both the type of upcoming service that will be required and when it will be required.

The new techniques described in this paper are based on two core elements of Cymer's light source data management architecture. The first is enhanced performance logging features added to newer-generation light source software that captures detailed performance data; and the second is Cymer OnLine (COL) which facilitates collection and transmission of light source data. Extensive analysis of the performance data collected using this architecture has demonstrated that many light source issues exhibit recognizable patterns in their symptoms. These patterns are amenable to automated identification using a Cymer-developed model-based fault detection system, thereby alleviating the need for detailed manual review of all light source performance information. Automated recognition of these patterns also augments our ability to predict the performance trending of light sources.

Such automated analysis provides several efficiency improvements for light source troubleshooting by providing more content-rich standardized summaries of light source performance, along with reduced time-to-identification for previously classified faults. Automation provides the ability to generate metrics based on a single light source, or multiple light sources. However, perhaps the most significant advantage is that these recognized patterns are often correlated to known root cause, where known corrective actions can be implemented, and this can therefore minimize the time that the light source needs to be offline for maintenance. In this paper, we will show examples of how this new tool and methodology, through an increased level of automation in analysis, is able to reduce fault identification time, reduce time for root cause determination for previously experienced issues, and enhance our light source performance predictability.

Keywords: light source, fault detection and classification, availability

Optical Microlithography XXIII, edited by Mircea V. Dusa, Will Conley, Proc. of SPIE Vol. 7640,
76402D · © 2010 SPIE · CCC code: 0277-786X/10/$18 · doi: 10.1117/12.852758

1. Introduction

The increasing cost sensitivity of semiconductor manufacturing is driving significant attention towards equipment uptime and availability. Particularly in leading edge lithography processes, the demand for uptime and availability cascades down to the litho tools which are the designed constraint in the manufacturing workflow. Improving uptime and availability means reducing equipment downtime, where downtime includes preventative maintenance and replacement of consumables, see SEMI E10 Standard [1] illustrated in Figure 1. Furthermore, one of the key elements in maximizing the availability efficiency is to minimize unscheduled downtime. While one solution would be to proactively replace consumables well before they cause unscheduled down time, the cost associated with premature replacement will negatively impact the overall operating costs.

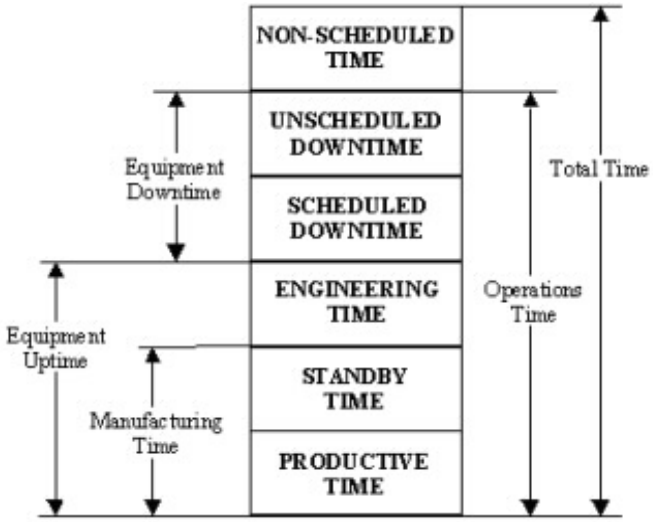

Figure 1: Breakdown of SEMI E10 standard (*Specification for Definition and Measurement of Equipment Reliability, Availability, and Maintainability*.)

Minimizing unscheduled downtime requires data to provide detailed analysis about tool performance to extend the consumable use and avoid premature replacements. In order to provide up-to-date information for troubleshooting and scheduling maintenance, while minimizing impact to the manufacturing process, tool performance data is collected on-line under production conditions. From the earliest excimer light sources, Cymer has collected extensive performance data from light sources that have been used to identify root cause for failures and create action plans for preventative maintenance. Recently, new techniques have been developed for more advanced automated data analysis to characterize the onset of end-of-life behavior of consumables and allow greater predictive capability for identifying when and what type of service will be required.

Comprehensive analysis of the performance data collected using this architecture has demonstrated that many light source issues exhibit recognizable patterns in their symptoms. These patterns are amenable to automated identification using a Cymer-developed model-based fault detection and classification (FDC) system, thereby alleviating the need for detailed manual review of all light source performance data. Furthermore, automated recognition of these patterns also augments the ability to predict performance trend of light sources.

Such automated analysis provides several efficiency improvements for light source troubleshooting and preventative maintenance scheduling by providing more content-rich standardized summarization of light source performance along with reduced time-to-identification for previously classified faults. Automation provides the ability to generate light source performance metrics based on the performance of a single light source, or of multiple light sources. However, perhaps the most significant advantage is that these recognized patterns are often correlated to a known root cause, where known corrective actions can be implemented. This can minimize the time that the light source needs to be offline for maintenance.

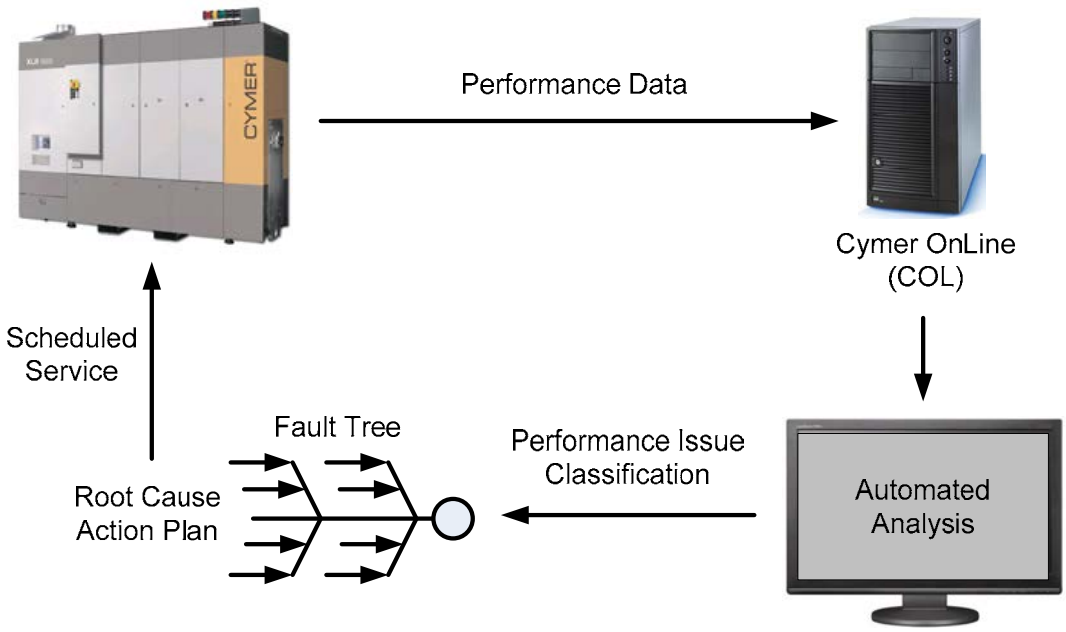
CYMER
Performance Data
Cymer OnLine
(COL)
Scheduled
Service
Fault Tree
Root Cause
Action Plan
Performance Issue
Classification
Automated
Analysis

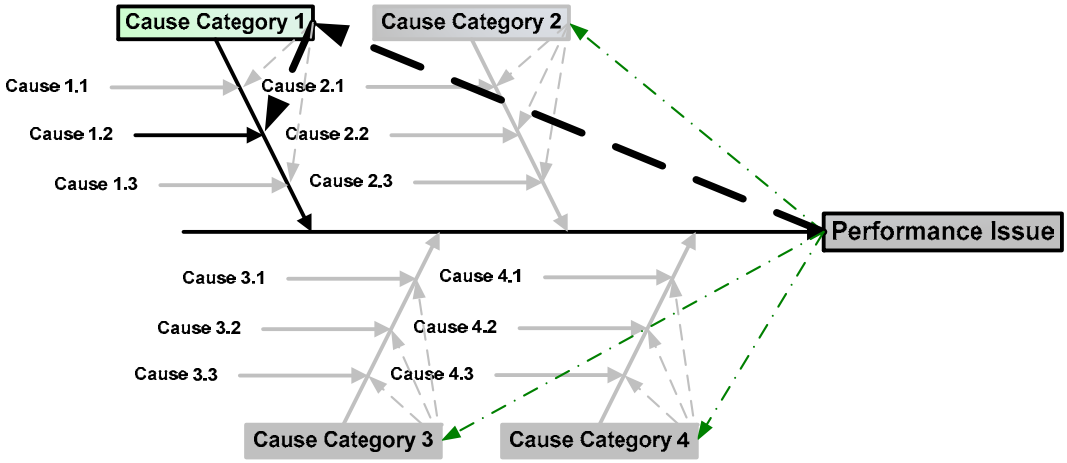
Cause Category 1
Cause Category 2
Cause 1.1
Cause 2.1
Cause 1.2
Cause 2.2
Cause 1.3
Cause 2.3
Performance Issue
Cause 3.1
Cause 4.1
Cause 3.2
Cause 4.2
Cause 3.3
Cause 4.3
Cause Category 3
Cause Category 4

upon a flexible infrastructure that enables rapid development and deployment of feature extraction mappings. Training data sets are used to evaluate feature extraction mappings over numerous light source operating conditions for effective and reliable identification of a particular fault condition. Once validated, newly developed features are easily deployed to the mainstream automated analysis software. Since the architecture relies on a centralized analysis function, software that resides on the fielded light sources does not need to be modified, and the implementation can be immediate.

For each light source performance data set received, multiple features can be extracted. The automated data analysis classifies the data set into a fault condition by observing all the extracted features and quantifying any discrepancies from expected behavior. Some fault conditions are amenable to single features that directly relate to root cause, while others require correlation of several features in order to recognize a pattern that indicates root cause. In either case, the automated analysis provides consistent information that reduces the reliance on expert service engineer judgment in identifying the correct resolution for a performance issue.

3.1 Case Study

The following case study provides an example for the methodology of the Cymer model-based FDC. The maximum pulse-to-pulse energy exceeds a specified threshold and triggers the fault condition (see Figure 4). Once the fault condition is detected, light source performance data is collected and transmitted for analysis as described in Section 2. Performing single-variate analysis, that is considering one signal at a time, the cause for the performance issue often can not be identified. Indeed several key signals, shown in Figure 5 – a and 5 – b, are well within their normal variation leading up to the fault condition.

Here it may be interesting to note that the fault condition presented in this case study is considered a rare occurrence. Particularly in known but rarely occurring fault events, detailed analysis beyond the readily available performance data (single-variate signals) would have required time and resources before issue resolution. Automating the data analysis expedites the troubleshooting processing by quickly delivering the relevant information about the fault symptoms regardless of how often the fault condition actually occurs.

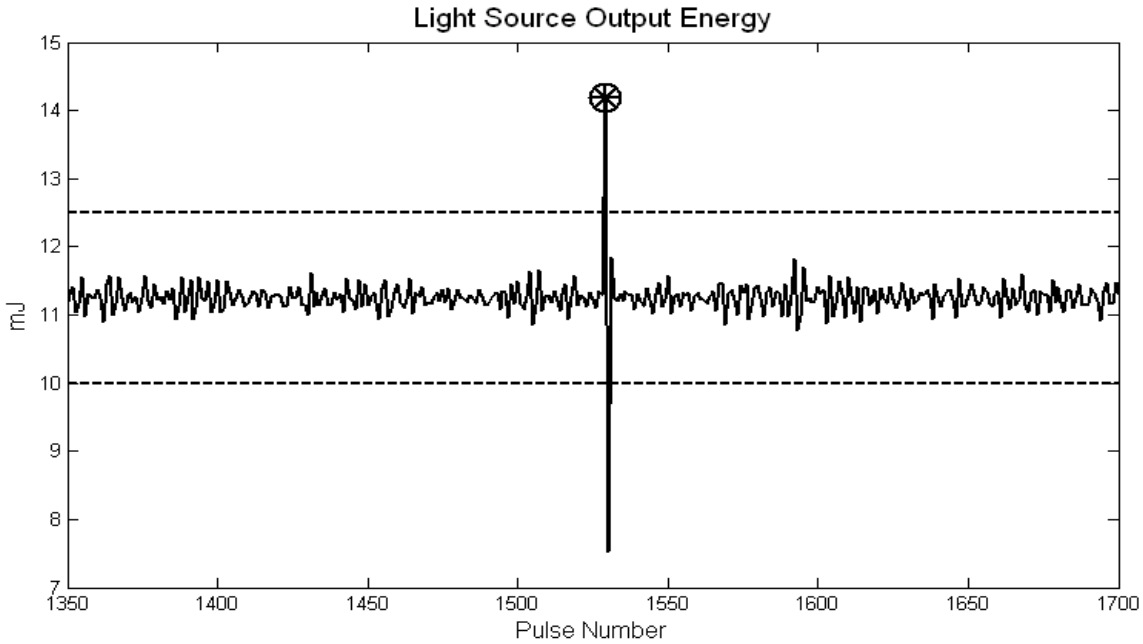

Figure 4: Light source measured output energy (solid line) is plotted against the pulse-to-pulse energy fault condition (dotted line). A pause in light source operation is indicated by the circle (O) which coincides with the first pulse to exceed the threshold designated by the marker (*).

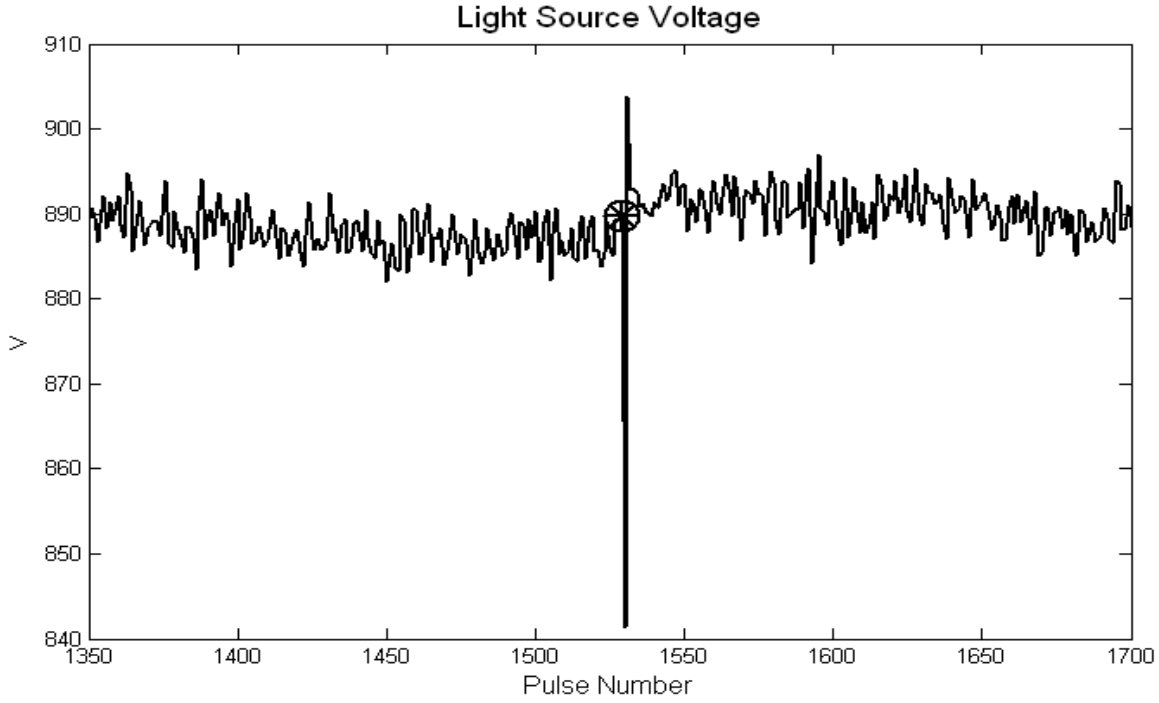

Figure 5 – a: Light source measured input voltage (solid line). A pause in light source operation is indicated by the circle (O) which coincides with the first pulse to exceed the threshold designated by the marker (*).

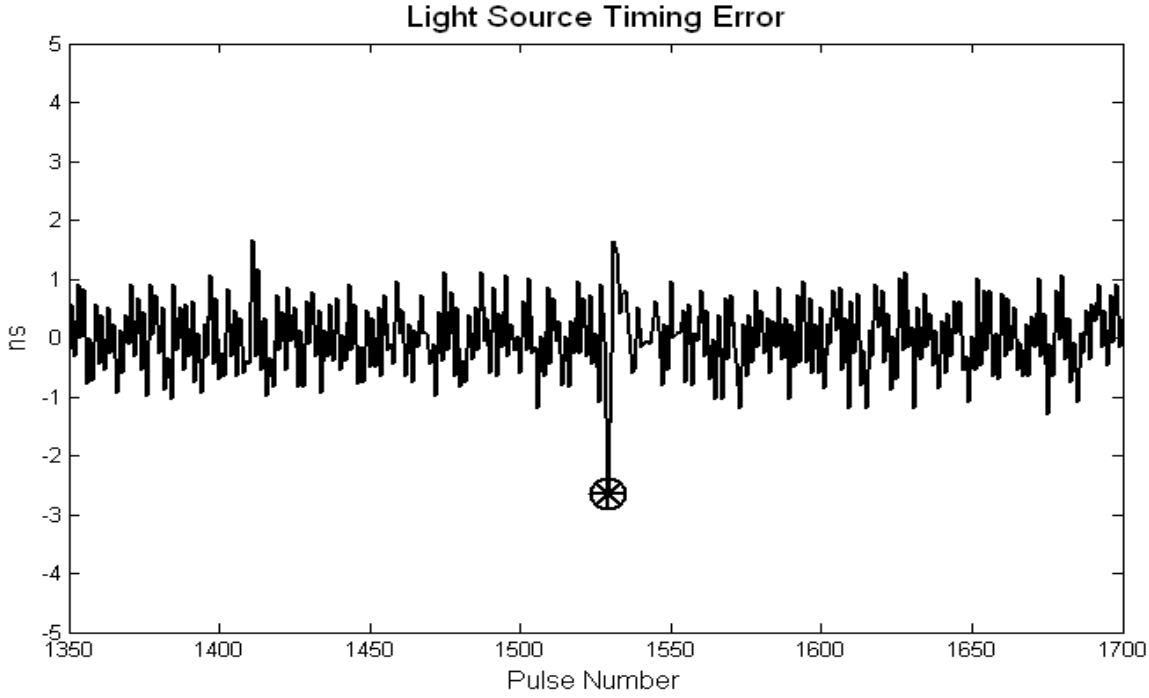

Figure 5 – b: Light source measured timing error (solid line). A pause in light source operation is indicated by the circle (O) which coincides with the first pulse to exceed the threshold designated by the marker (*).

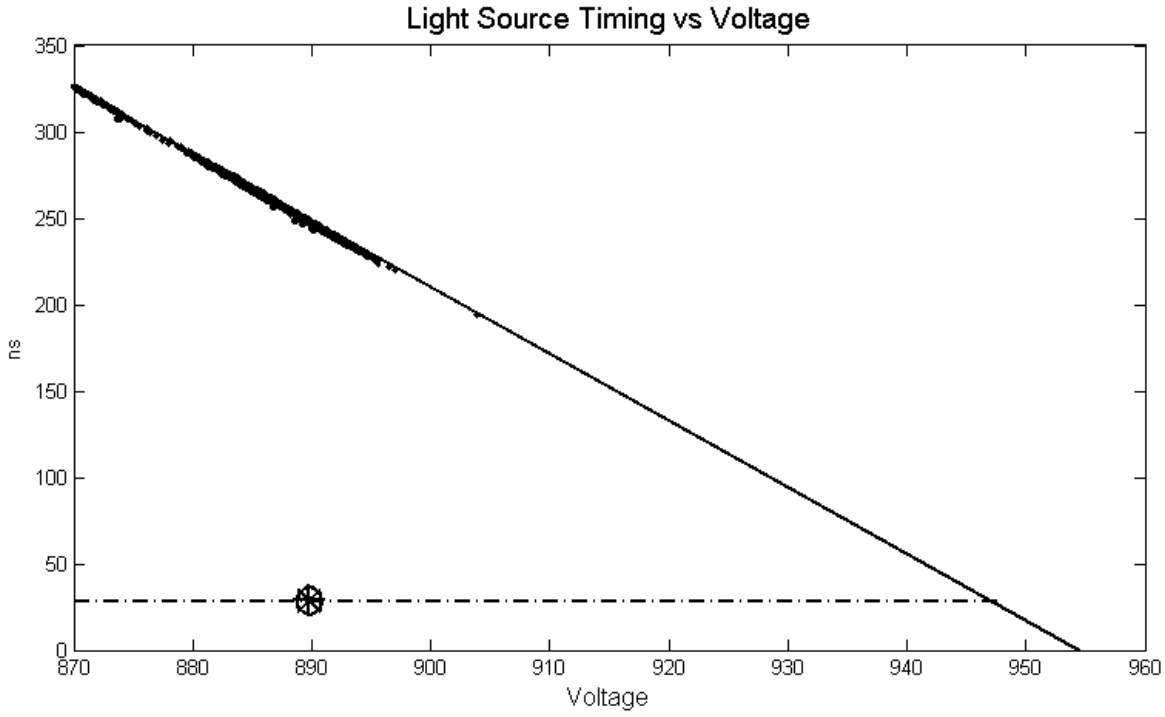
Light Source Timing vs Voltage
ns
Voltage
350
300
250
200
150
100
50
0
870
880
890
900
910
920
930
940
950
960

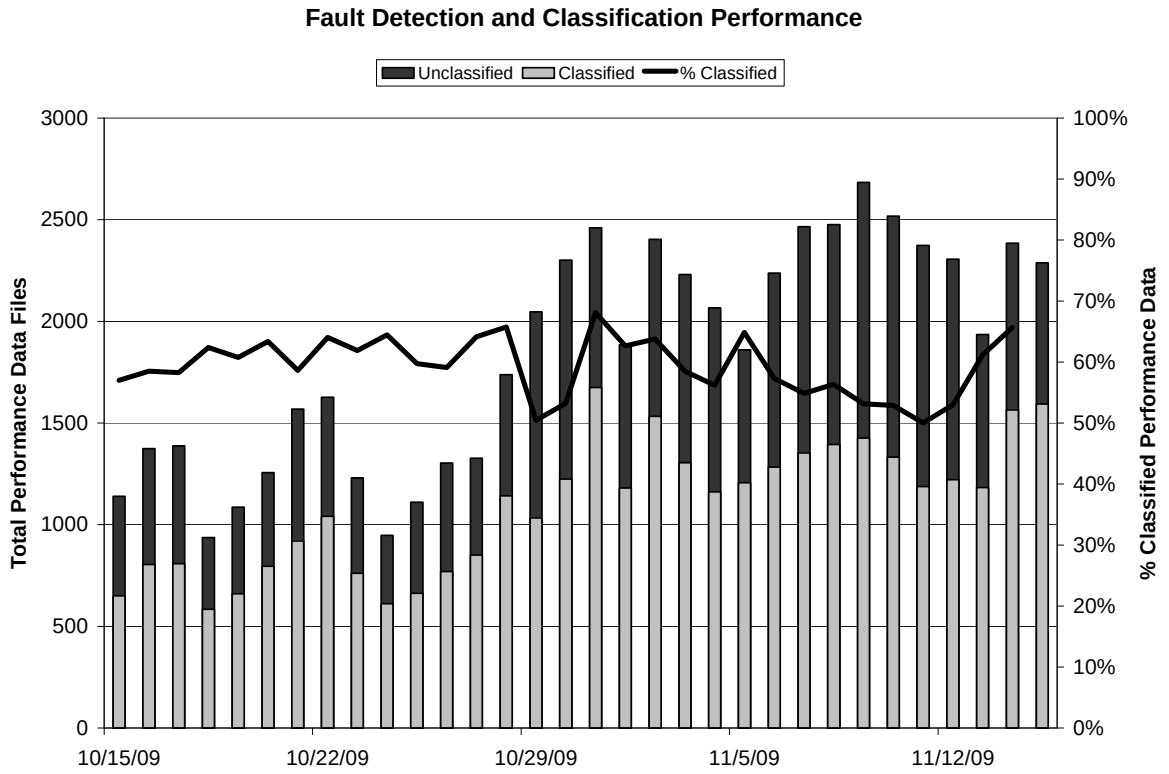

Figure 7: FDC performance in monitoring all fielded Cymer light sources. On average, 60% of performance issues are classified.

As mentioned in Section 2, the Cymer FDC system enhances current service strategy and augments the ability to predict the performance trending of light sources. Many fault conditions progress with operation of the light source, thus by monitoring the performance data issues can be recognized and addressed more accurately and with more time to prepare scheduled maintenance action plans. Consider for example the performance issue presented in Figure 8. The fault condition was automatically identified prior to customer impact and the appropriate action plans were developed and ready for the next scheduled maintenance opportunity. The performance issue caused by the fault condition was resolved during scheduled maintenance, reducing the impact to production.

As a part of an overall service strategy, automated FDC augments the ability to predict the performance trending of light sources. The impact of augmenting performance predictability can be observed in comparing scheduled versus unscheduled downtime. Cymer Technical Support deployed a Proactive Service Program (PSP) in conjunction with FDC in December 2008. The FDC system adds information performance summaries for each light source. Figure 9 shows the monthly scheduled versus unscheduled events for one customer participating in this program. Shortly after deployment, the ratio between scheduled versus unscheduled service improved by 10%. While there are many factors that contribute to this improvement, FDC enhances the capabilities and value of the Cymer PSP program.

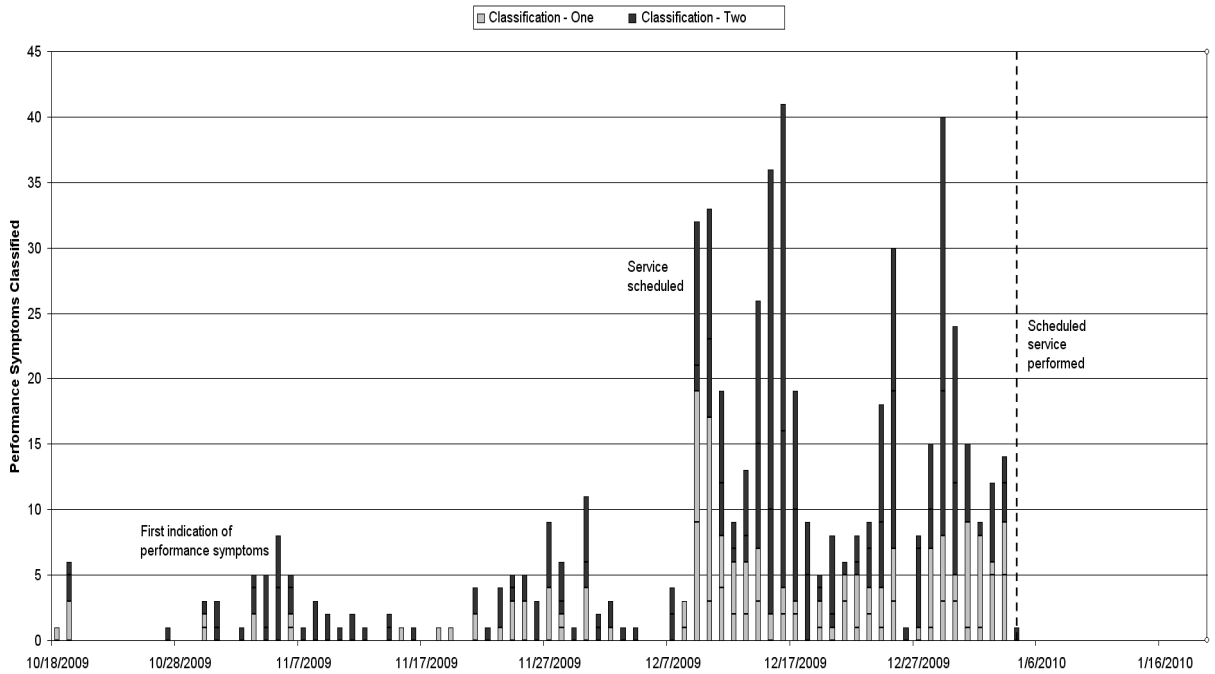

Figure 8: FDC summary for a single light source during the progression of performance symptoms. The performance symptoms begin with small low rate of events that increase in frequency over time. Two classification types, which are related to a single light source subsystem, have been identified. In this case, automated classification enabled awareness of the performance issue root cause with sufficient time to schedule maintenance with two week horizon.

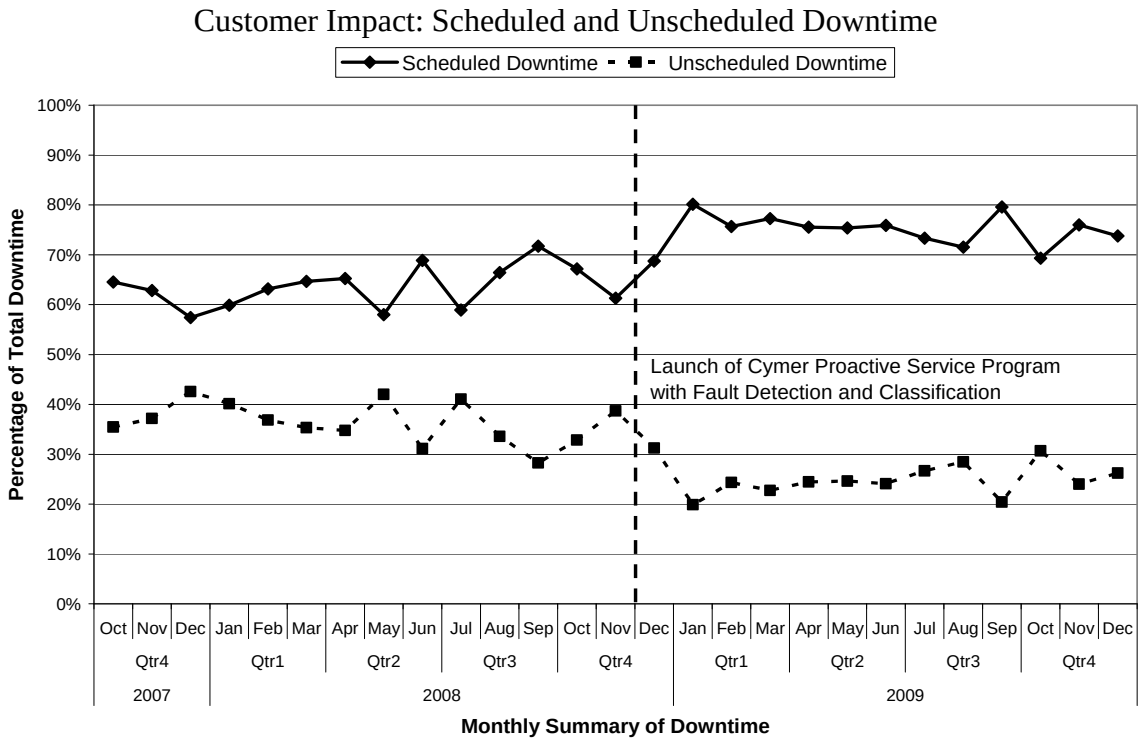

Figure 9: Single customer comparison of scheduled versus unscheduled downtime that shows the improvement in scheduled service with the deployment of Proactive Service Program (PSP) in conjunction with FDC.

5. Conclusions and Future Work

Cymer FDC provides several efficiency improvements for light source troubleshooting by providing more content-rich standardized summaries of light source performance along with reduced time-to-identification for previously classified faults. Perhaps the most significant advantage is that performance issues that exhibit recognized patterns are often correlated to known root cause, where known corrective actions can be implemented. This is therefore used to schedule service activities and minimize the impact of the duration of time that the light source is offline for maintenance. Through an increased level of automation in analysis, Cymer is able to reduced fault identification time, reduce time for root cause determination for previously experienced issues, and enhance light source performance predictability.

References

[1] SEMI E10 - for Definition and Measurement of Equipment Reliability, Availability, and Maintainability.

[2] Isermann, R. "Model-based fault detection and diagnosis – status and applications" Annual Reviews in Control, 29(1), 71-85, (2005).

[3] Jain, A.K., Duin, R.P.W., Mao, J. "Statistical pattern recognition: A review" IEEE Transactions on Pattern Analysis and Machine Intelligence, 22 (1), 4-37, (2000).

LPP Source System Development for HVM

David C. Brandt*, Igor V. Fomenkov, Alex I. Ershov, William N. Partlo, David W. Myers
Richard L. Sandstrom, Norbert R. Böwering, Georgiy O. Vaschenko, Oleh V. Khodykin, Alexander N. Bykanov,
Shailendra N. Srivastava, Imtiaz Ahmad, Chirag Rajyaguru, Daniel J. Golich, Silvia De Dea, Richard R. Hou,
Kevin M. O'Brien, Wayne J. Dunstan

Cymer Inc., 17075 Thornmint Court, San Diego, CA 92127, USA

ABSTRACT

Laser produced plasma (LPP) systems have been developed as a viable approach for the EUV scanner light source to support optical imaging of circuit features at sub-22nm and beyond nodes on the ITRS roadmap. This paper provides a review of development progress and productization status for LPP extreme-ultra-violet (EUV) sources with performance goals targeted to meet specific requirements from leading scanner manufacturers. The status of first generation High Volume Manufacturing (HVM) sources in production and of prototype source operation at a leading scanner manufacturer is discussed. The EUV power at intermediate focus is discussed and the lastest data is presented. An electricity consumption model is described, and our current product roadmap is shown.

Keywords: EUV source, EUV lithography, Laser Produced Plasma

1. INTRODUCTION

EUV Lithography is the front runner for next generation critical dimension imaging after 193 nm immersion lithography for layer patterning below the 32 nm node; beginning in 2013 according to the International Technology Roadmap for Semiconductors (ITRS). NAND Flash devices are expected to have the need for this manufacturing technology as soon as 2011, with pilot line system introduction starting this year (2010). The availability of high power 13.5 nm sources has been categorized as high risk and ranked as critical with other technologies requiring significant developments to enable the realization of EUV lithography. High sensitivity photoresists with good line-edge-roughness (LER) and line-width-roughness (LWR) are needed to keep the required source power within reasonable limits. Photoresist sensitivity and overall optical transmission through the EUV scanner are the basis to derive EUV source power requirements within the usable bandwidth (BW) of 2 %. Scanner manufacturers are requiring clean EUV power close to 200W at the intermediate focus (IF) to enable > 100 wph scanner throughput assuming 10 mJ/cm^2 photoresist sensitivity. The need for a spectral purity filter (SPF) increases the requirements for raw EUV Power even higher. Clean EUV Power is calculated by taking the raw EUV power and subtracting the losses associated with the spectral purity filter (SPF) and dose control, for initial sources these losses are estimated to be 35% and 20% respectively. A scalable EUV source architecture is needed to enable the evolution of EUV lithography during the life cycle of the technology. Laser-produced-plasma (LPP) sources are expected to deliver the necessary power for critical-dimension high-volume manufacturing (HVM) scanners for the production of integrated circuits in the post-193 nm immersion era.[1]

LPP EUV lithography light sources generate the required 13.5 nm radiation by focusing a 10.6 micron wavelength CO_2 laser beam into tin (Sn) creating a highly ionized plasma with electron temperatures of several 10's of eV. EUV photons are radiated isotropically by these ions. Photons are collected with a normal-incidence mirror (collector), and focused to an intermediate point from where they are relayed to the scanner optics and ultimately to the wafer. High conversion efficiency (CE) of the laser energy into EUV energy is critical to meeting the required power levels. A prototype configuration based on this approach was shipped to a leading scanner manufacturer in 2009. The normal-incidence mirror is protected from the plasma by hydrogen buffer gas debris mitigation technology. High-energy ions, fast neutrals, and residual source element particles are mitigated to maintain the reflectivity of the collector mirror and enable a long lifetime of this component. Diagnostics measuring the properties of emitted light at both the plasma and IF are

used to characterize the output of the source.[2] Performance results of test and prototype light sources obtained up to about a year ago have already been described in detail previously.[1,3,4,5]

2. LPP SOURCE SYSTEM

The system architecture is show schematically in Figure 1. The three major subsystems of the source are the drive laser, the beam transport system (BTS) and the source vessel. The drive laser is a CO_2 laser with multiple stages of amplification to reach the required power level of ~20 kW.[1,6] It is operated in pulsed mode at ~50 kHz with radio-frequency (RF) pumping from generators (not shown) operating at 13.56 MHz. The laser is typically installed in the sub-fab along with its RF generators and water-to-water heat exchangers. The source controller turns on and off bursts of pulses, which can be as long as several seconds, but is typically 400ms for exposing a 26 x 33mm field size using 10mJ/cm^2 resist. The ratio of time when the burst is on to the burst period defines the duty cycle. The beam is expanded as it leaves the drive laser to maintain the energy density on the BTS mirrors within a certain operating range. Three turning mirrors are used to allow the beam to travel from the sub-fab to the fab through the waffle-slab floor with the needed flexibility for positioning the laser with respect to the source vessel (and scanner) on the floor above. The laser and BTS are completely enclosed and interlocked to meet laser class 1 requirements. The BTS delivers the beam to a focusing optic where the 10.6 micron wavelength light is focused to a minimum spot size defined by the numerical aperture of the focusing system. The focused beam propagates through a central aperture in the collector and strikes the droplet at the focus of the ellipsoidal collector mirror inside the vacuum space of the source vessel chamber. The droplet generator delivers liquid tin droplets of 30 micron diameter to the same position at ~ 50 kHz repetition rate; both laser pulse and droplets are steered and timed to ensure proper targeting. The laser pulse vaporizes and heats the tin into a plasma cloud of critical temperature and density. The EUV light emitted by the plasma is collected and reflected with the multi-layer coated ellipsoidal mirror to the intermediate focus (IF) where it passes through a small aperture into the scanner volume that houses the illumination optics. To ensure that no contamination can reach the scanner volume an IF protection module surrounds the aperture and suppresses flow or diffusion. Other modules on the source vessel include the droplet catcher which collects the unused droplets between the bursts, and metrology modules for measuring EUV energy and for imaging of droplets and plasma.

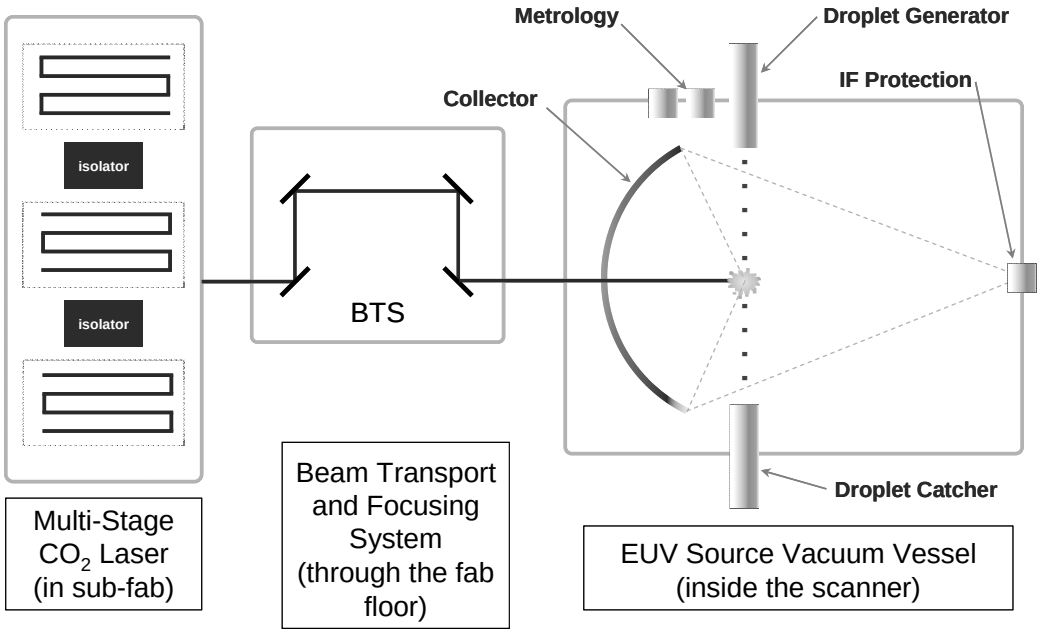

Figure 1: Schematic of Laser Produced Plasma Source.

Six first-generation high-volume manufacturing (HVM I) sources are presently in production in the cleanroom in our San Diego California facility. A source vessel is shown in Figure 2 positioned at specified source orientation angle, and the drive laser for this source is shown in Figure 3. The BTS connects the two major modules through the wall. The first three sources are operational and their performance is being optimizeed to complete acceptance testing for our customers.

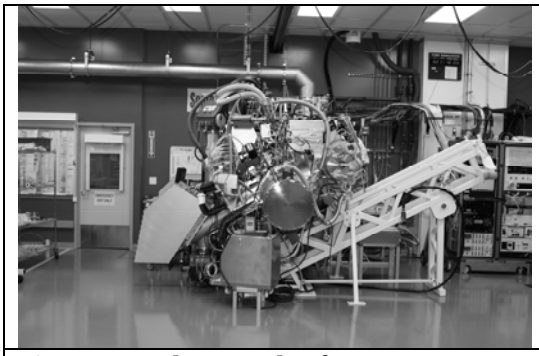

Figure 2: Photograph of a HVM I LPP Source Vessel in production.

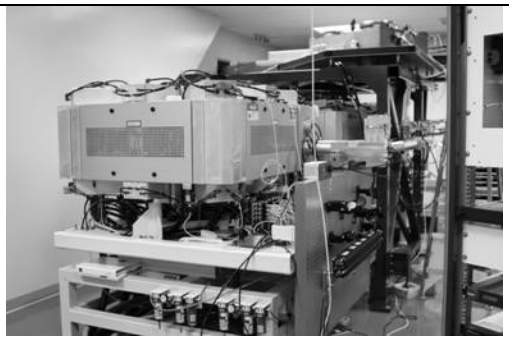

Figure 3: Photograph of a HVM I LPP Source CO_2 Drive Laser in production.

3. RECENT DEVELOPMENT RESULTS

Figure 4 shows the raw EUV power obtained at our Engineering Test Stand LPP source[7] running at 80% duty cycle, as determined from measurements at plasma. IF-equivalent average powers above 90W were reached using standard assumptions of 50% reflectivity for a 5 sr collector and for 90% optical transmission from plasma to IF. The power level was reached using a laser configuration with longer gain length compared to our standard production system and demonstrates the expected performance of the planned upgrade to HVM I sources. The open loop energy stability of a 10ms sliding window through the raw data is 5.4% (3σ) is also shown. An estimated EUV power of 80W will be achieved by applying closed-loop dose control. These experiments were performed using tin droplets with 30 micron diameter at 50kHz repetition rate and 400ms burst duration, the standard production system parameters for our HVM I sources.

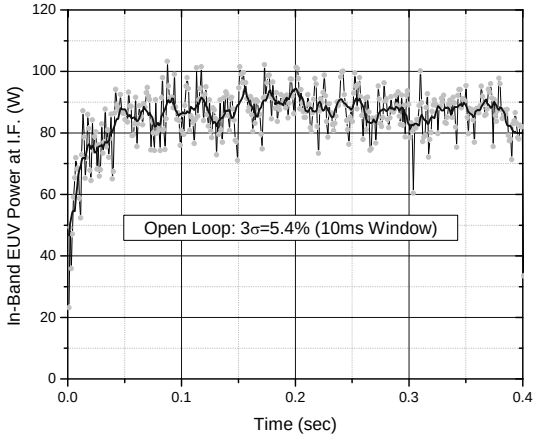

Figure 4: ~90W raw EUV Power at IF obtained in a 400ms burst at 80% duty cycle on 30μm diameter Sn droplets.

Figure 5 and Figure 6 show views of our prototype LPP system integrated with a test fixture in the cleanroom at our customer. This full-size prototype LPP source with basic controls was built in 2008 and shipped in 2009. It was operated in our San Diego facility for about nine months before being transferred to the customer. The maximum EUV power produced on this source was ~45W at IF. Our debris mitigation technology using hydrogen buffer gas was validated on this system using a 5sr collector. The installation at ASML took about three months and the source became operational in September 2009. It has been used for numerous functional tests and integration operations in the months since, including testing of the SPF and its ability to filter out of band IR light. The primary use of the source has been for testing sensors, controls algorithms and interfaces, and diagnostics. Its typical performance as installed is ~10W raw EUV power at IF and ~7W when under dose control (~1.0% stability). The plasma position stability has been measured to be within the specification of ±10μm when under feedback control. The far field EUV intensity distribution from the source has been monitored using a diagnostics tool inserted into the optical path beyond IF.

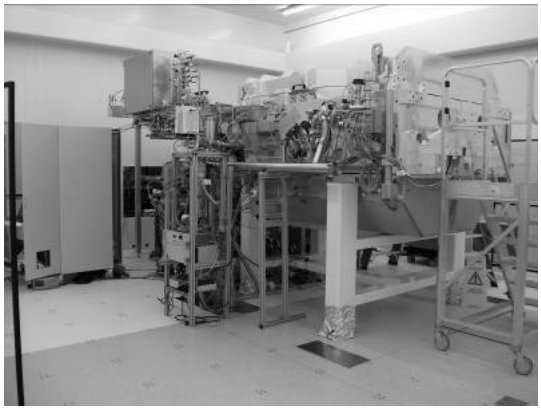

Figure 5: Mid frame vessel housing illumination optics.

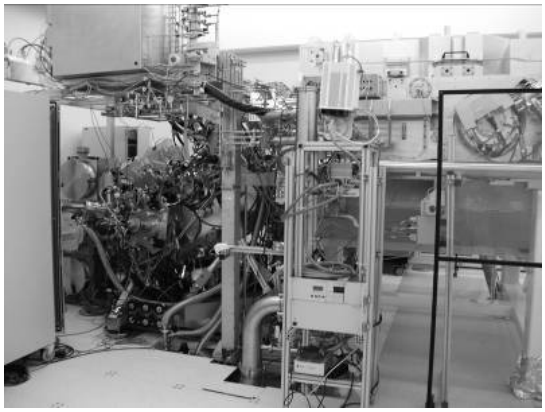

Figure 6: Prototype LPP source integrated with the mid frame vessel.

4. ELECTRICITY CONSUMPTION

A major utility for the EUV source is the electrical power that the system requires. With the operation of the EUV source at nominal scanner operating conditions, we can estimate with reasonable certainty the amount and cost of the electrical power used. These calculations are shown in Table 1. The roadmap for additional EUV power actually predicts a decreasing cost of electrical consumption. Despite higher throughput tools and greater EUV power, this decreased cost is obtained by the more efficient utilization of the available EUV light. A reduced percentage of source on-time is required for the exposure as the duty cycle of the source is reduced, resulting in a lower usage of electrical consumption and a lower cost. It should be noted that the cost of electricity consumption used here was based on 0.09 $/kWhr. Compared to a 193nm immersion light source such as Cymer's XLR 600ix with a power consumption of 85kVA the LPP EUV source consumption is approximately three times greater for equivalent throughput.

	193nm (XLR 600ix)	**EUV (HVM I)**	**EUV (HVM II)**	**EUV (HVM III)**
Source Output Power, Clean EUV (W)	60	100	250	350
Duty Cycle (%)	26%	73%	39%	31%
Source Input Power, Electricity (kVA)	85	448	321	292
Cost of Electricity ($/kWhr)	0.09	0.09	0.09	0.09
Cost of Electricity ($1000/yr)	47	247	177	161

Table 1: Estimated usage and cost of electrical power.

5. ROADMAP

Currently, our HVM I sources are undergoing acceptance testing. HVM I source designs are based on the learning obtained from prototype sources and technology developed on our internal Engineering Test Stand. The LPP source roadmap is shown in Table 2. The HVM I product is expected to meet requirements for pre-production or beta generation scanners in 2010 with clean EUV output powers of >100 W using a 25 kW CO_2 laser system on Sn droplets with 3.0 % CE. The normal-incidence collectors used have a collection solid angle of ~ 5 sr and multilayer coatings with EUV reflectivity > 50 % on average over the surface. Transmission losses due to absorption and debris mitigation techniques are projected to be less than 20 %. It is expected that requirements for later generation LPP EUV sources will drive source powers above the 350 W level (HVM III) with CO_2 laser technology delivering ~37 kW of power. Further improvements in CE and collection efficiency are expected to enable clean EUV power levels exceeding 400W at IF.

EUV Source Power Roadmap			
	HVM I	HVM II	HVM III
Drive Laser Power (kW)	**25**	**35**	**37**
In-band CE (%)	3.0	3.5	4.0
Collection Efficiency (sr)	5	5.5	5.5
Collector Reflectivity (%)	50	50	50
Clean EUV Power (W)	**>100**	**>250**	**>350**

Table 2: Projected LPP EUV source roadmap

6. SUMMARY

Laser-produced plasmas have been shown to be the leading source technology with scalability to meet requirements from leading scanner manufacturers and provide a path toward higher power as the lithography tools evolve over their life cycle. EUV power exceeding 90W at intermediate focus at 80% duty cycle and 400ms burst length has been reported. Normal-incidence collector mirrors of diameter > 650mm, with > 5 sr light collection and average reflectivity >50% are produced and integrated into production LPP systems. The high-conversion-efficiency combination of 10.6 μm laser light and Sn source element has been demonstrated with CE in excess of 3 %. LPP source technology with power levels exceeding 400W is expected to satisfy the IF power requirement projected in the future, and to provide margins for changes in photoresist sensitivity, spectral purity filters transmission, and overall scanner transmission. Cymer intends to commercialize EUV light sources in 2010.

ACKNOWLEDGEMENTS

The authors gratefully acknowledge the valuable contributions from Martin J. Neumann and David N. Ruzic of University of Illinois, Urbana Champaign, Marco Perske, Hagen Pauer, Mark Schürmann, Sergiy Yulin, Torsten Feigl and Norbert Kaiser of Fraunhofer Institut f. Angewandte Optik und Feinmechanik, Eric Gullikson and Farhad Salmassi of Lawrence Berkeley National Laboratory, Frank Scholze, Christian Laubis, Christian Buchholz and coworkers at PTB, and Mark Tillack and Yezheng Tao of the University of California at San Diego. We are also very thankful for the invaluable support and contributions, past and present, of many scientists, engineers and technicians involved in the EUV technology program at Cymer.

REFERENCES

[1] I. V. Fomenkov, D. C. Brandt, A. N. Bykanov, A. I. Ershov, W. N. Partlo, D. W. Myers, N. R. Böwering, G. O. Vaschenko, O. V. Khodykin, J. R. Hoffman, E. Vargas L., R. D. Simmons, J. A. Chavez, C. P. Chrobak, in: *Proc. of SPIE Vol. **6517**, Emerging Lithographic Technologies XI*, M. J. Lercel, ED., 65173J (2007).

[2] N. R. Böwering, J. R. Hoffman, O. V. Khodykin, C. L. Rettig, B. A. M. Hansson, A. I. Ershov, I. V. Fomenkov, in: *Proc. SPIE **Vol. 5752**, Metrology, Inspection, and Process Control for Microlithograpy XIX*, R. M. Silver, Ed., 1248-1256 (2005).

[3] D. C. Brandt, I. V. Fomenkov, A. I. Ershov, W. N. Partlo, D. W. Myers, N. R. Böwering, N. R. Farrar, G. O. Vaschenko,O. V. Khodykin, A. N. Bykanov, J. R. Hoffman, C. P. Chrobak, S. N. Srivastava, I. Ahmad, C. Rajyaguru, D.J. Golich, D. A. Vidusek, S. De Dea, R. R. Hou, in: *Proc. of SPIE Vol. **7271**, Alternative Lithographic Technologies*, F. M. Schellenberg, B. M. La Fontaine, Eds., 727103, (2009).

[4] I. V. Fomenkov, D. C. Brandt, A. N. Bykanov, A. I. Ershov, W. N. Partlo, D. W. Myers, N. R. Böwering, N. R. Farrar, G. O. Vaschenko, O. V. Khodykin, J. R. Hoffman, C. P. Chrobak, S. N. Srivastava, D.J. Golich, D. A. Vidusek, S. De Dea, R. R. Hou, in: *Proc. of SPIE Vol. **7271**, Alternative Lithographic Technologies*, F. M. Schellenberg, B. M. La Fontaine, Eds., 727138 (2009).

[5]N. R. Böwering, I. V. Fomenkov, D. C. Brandt, A. N. Bykanov, A. I. Ershov, W. N. Partlo, D. W. Myers, N. R. Farrar, G. O. Vaschenko, O. V. Khodykin, J. R. Hoffman, C. P. Chrobak, S. N. Srivastava, I. Ahmad, C. Rajyaguru, D.J. Golich, D. A. Vidusek, S. De Dea, R. R. Hou, Journal of Micro/Nanolith. MEMS MOEMS 8(4), 041504 (2009).

[6] I. V. Fomenkov, B. A.M. Hansson, N. R. Böwering, A. I. Ershov, W. N. Partlo, V. B. Fleurov, O. V. Khodykin, A. Bykanov, C. L.Rettig, J. R. Hoffman, E. Vargas L., J. A. Chavez, W. F. Marx, D. C. Brandt, in: *Proc. of SPIE Vol. **6151**, Emerging Lithographic Technologies X*, M. J. Lercel, Ed., 61513X (2006).

[7] D. C. Brandt, I. V. Fomenkov,, A. I. Ershov, W. N. Partlo, D. W. Myers, N. R. Böwering, A. N. Bykanov, G. O. Vaschenko, O. V. Khodykin, J. R. Hoffmann, E. Vargas L., R. D. Simmons, J. A. Chavez, C. P. Chrobak, in: *Proc. of SPIE Vol. **6517**, Emerging Lithographic Technologies XI*, M. J. Lercel, ED., 65170Q (2007).